TERT drives liver tumorigenesis beyond telomere elongation

Laura Braud[1], Julien Vernerey[1], Arnaud Guille[2], Pierre Cordier[3], Clémence Ginet[4], Tom Egger[5], Manuel Bernabe[1], Dmitri Churikov[1], Quentin Da Costa[2], Aïda Meghraoui[4], Chantal Desdouets[3], Li Gu[6], François Bertucci[2], Christophe Lachaud[7], Vincent Géli[1,8,*]

[1] CRCM, Inserm, CNRS, Institut Paoli-Calmettes, Aix-Marseille University Marseille, France. Équipe labellisée par la Ligue Nationale Contre le Cancer.
[2] Predictive Oncology Laboratory, Marseille Cancer Research Centre (CRCM), Inserm U1068, CNRS UMR7258, Institut Paoli-Calmettes, Aix-Marseille University, Marseille, France
[3] Centre de recherche des Cordeliers, Sorbonne université, Inserm, Université Paris Cité, Paris, France . Équipe labellisée par la Ligue Nationale Contre le Cancer.
[4]AMKbiotech, BIOPARC, Biot, France
[5]Quantimagin, Montpellier, France.
[6]Department of Laboratory Medicine and Clinical Laboratory Medicine Research Center, West China Hospital, Sichuan University, Chengdu, China.
[7]CRCM, Inserm, CNRS, Institut Paoli-Calmettes, Aix-Marseille University, DNA Interstrand Crosslink Lesions and Blood Disorder Team, Marseille, France
[8]Institute for Research on Cancer and Aging of Nice (IRCAN), Université Côte d'Azur, INSERM, CNRS, Nice, France.

*Corresponding author: vincent.geli@inserm.fr tel: 33 6 76 47 89 00

Keywords: TERT, Hepatocellular carcinoma mouse model, p21, mutagenesis, metabolic reprogramming, HNF4alpha

Abstract

We generated two mouse models, $p21^{+/Tert}$ and $p21^{+/TertCi}$, expressing either telomerase reverse transcriptase (TERT) or a catalytically inactive variant under the control of the p21 promoter. By 18–20 months of age, approximately 25% of mice from both genotypes developed liver tumors with histopathological features resembling human hepatocellular carcinoma (HCC). Whole-exome sequencing identified activating Ctnnb1 mutations and recurrent PP1 subunit alterations in $p21^{+/Tert}$ tumors, whereas $p21^{+/TertCi}$ tumors harbored activating $Hras^{Gln61Lys}$ mutations associated with elevated C>A transversions. Both models exhibited chromosomal aberrations commonly observed in human HCC. Transcriptomic analyses revealed that β-catenin–activated tumors recapitulated gene expression signatures of human HCC, while MAPK-mutated tumors showed profiles consistent with MAPK/ERK pathway activation. Metabolically, both genotypes demonstrated increased glycolysis and suppression of gluconeogenesis, including downregulation of FBP1, but expressed distinct NRF2 target genes. Spatial profiling further revealed reduced HNF4α-positive hepatocytes across tumors, independent of Hnf4α transcription, and markedly diminished immune cell infiltration particularly in β-catenin–activated tumors. Collectively, these findings uncover telomere-independent functions of TERT and identify molecular and metabolic features with potential relevance for predicting immunotherapy response.

Introduction

Hepatocellular carcinoma (HCC) is the third leading cause of cancer-related mortality worldwide. It arises in the setting of chronic liver diseases such as chronic hepatitis B or C infection, cirrhosis, and metabolic syndrome which are frequently accompanied by persistent inflammation (Zucman-Rossi *et al*, 2015; Nault *et al*, 2019). Within this pathological environment, the accumulation of driver mutations leads to the disruption of key signaling pathways, ultimately driving hepatocarcinogenesis (Schulze *et al*, 2015). Among the most frequently deregulated are the Wnt/beta-catenin and p53 pathways (Rebouissou *et al*, 2016; Fujimoto *et al*, 2015). In addition, multiple other pathways contribute to HCC development, including recurrent amplifications of MYC and cyclin-dependent kinase genes, and mutations that activate the Sonic Hedgehog, RAS/MAPK, PI3K-Akt, and oxidative stress response pathways (Chen *et al*, 2010; Delire & Stärkel, 2015; Zhang *et al*, 2016).

Frequent mutations in hepatocellular carcinoma (HCC) occur early in carcinogenesis within the promoter region of the TERT gene, which encodes the catalytic subunit of telomerase (Nault *et al*, 2013, 2014). Various genetic and epigenetic mechanisms, including TERT promoter mutations, hepatitis B virus integration, chromosomal rearrangements, and promoter methylation changes, lead to aberrant upregulation of TERT in the majority of HCC cases (Totoki *et al*, 2014). Traditionally, telomerase reactivation in HCC is considered as a compensatory response to critical telomere shortening preventing senescence and apoptosis especially in cells harboring p53 mutations (Farazi *et al*, 2006). However, emerging evidence indicates that TERT also performs non-canonical functions beyond telomere elongation that may promote tumorigenesis (Ségal-Bendirdjian & Geli, 2019). Depending on cellular context, TERT has been implicated in the regulation of major oncogenic pathways, including WNT/beta-catenin, NF-κB, and MYC (Park *et al*, 2009; Ghosh *et al*, 2012; Koh *et al*, 2015). Recent studies in murine models of chronic liver inflammation have shown that TERT can enhance NF-κB promoter activity and drive liver tumor formation, particularly in the absence of functional p53 (Mishima *et al*, 2024). Despite these findings, the non-canonical roles of TERT in HCC remain poorly understood.

We developed two related mouse models, $p21^{+/Tert}$ and $p21^{+/TertCi}$, in which either wild-type TERT or a catalytically inactive TERT mutant ($TERT^{Ci}$) is expressed under the control of the *Cdkn1a* (p21) promoter. This strategy was designed to establish a tightly regulated feedback loop, enabling telomerase expression specifically in p21-positive cells. Unexpectedly, we found that both TERT and TERTCi suppress p21 expression and attenuate cellular senescence either in the lungs of aged mice (Lipskaia *et al*, 2024) or in the adipose tissue of young obese mice fed a high-fat diet (Braud *et al*, 2025). These results suggest that TERT can inhibit senescence through mechanisms independent of its canonical telomere-lengthening activity. Overall, the $p21^{+/Tert}$ and $p21^{+/TertCi}$ models promote TERT expression in pre-senescent cells and facilitate senescence bypass, an early event frequently associated with tumor initiation, particularly in the liver. In this study, we demonstrate that 15% of $p21^{+/Tert}$ and $p21^{+/TertCi}$ mice develop liver tumors by 18 months of age, exhibiting characteristics closely resembling those of human hepatocellular carcinoma (HCC). Through these two mouse models, we identify a telomere-independent role for TERT in liver tumorigenesis and immune modulation. These findings reveal non-canonical TERT functions and highlight molecular and metabolic biomarkers relevant to HCC pathogenesis and immunotherapy response.

Results

$p21^{+/Tert}$ and $p21^{+/TertCi}$ mice develop hepatocellular carcinomas with features of human HCC

We found that by 18–20 months of age, both $p21^{+/Tert}$ and $p21^{+/TertCi}$ mice predominantly developed liver tumors. We were surprised to find that mice expressing the catalytically inactive $TERT^{Ci}$ developed liver tumors with similar frequency to those expressing active telomerase. The majority of these tumors were of hepatocellular origin and identified as hepatocellular carcinomas (HCC) or hepatocellular adenomas (HCA). A number of hematological malignancies and liver hemangiosarcomas were also observed (Table 1, Figure 1).

We focused our analysis on hepatocellular tumors, given their predominance. HCCs in $p21^{+/Tert}$ and $p21^{+/TertCi}$ mice exhibited histomorphological features reminiscent at least to some extent of human HCCs. In general, we noted in most liver tumors, as it is the case for human HCC, a nodular to multi-nodular hepatocellular neoplastic lesion with loss of lobular architecture leading to destruction and rarefaction of adjacent parenchyma, although overt tumor invasion was more difficult to identify (Table 1). The murine HCCs were not encapsulated. We found that the growth pattern of HCCs in the transgenic mice was most often 'micro-*trabecular*' (neoplastic hepatocytes forming multiple-cell-thick trabeculae alternating with sinusoidal capillaries), or '*solid*' (continuous range of neoplastic hepatocytes with very little tumor stroma), with a frequent combination of both patterns within the same tumor (Table 1). These observations are in agreement with the histopathological aspects of human HCC, in which both growth patterns can be found alone or in association. Likewise, the liver tumors from $p21^{+/Tert}$ and $p21^{+/TertCi}$ mice showed multifocal areas of necrosis, hemorrhage or angiectasia. Of note, other tumor growth patterns described in humans (pseudoglandular, macrotrabecular, scirrhous, etc.) were not observed in the $p21^{+/Tert}$ and $p21^{+/TertCi}$ models. Tumor hepatocytes in both mouse models remained well-differentiated (mimicking mature hepatocytes) with a central round euchromatic nucleus and moderately abundant to markedly abundant granular eosinophilic cytoplasm (Table 1), thus resembling low-grade human HCCs. Accordingly, cellular atypia was mostly mild to moderate with increased nuclear–cytoplasmic ratio, anisokaryosis and occasional karyomegaly and nuclear pleomorphism. In some tumors, neoplastic hepatocytes showed prominent cytoplasmic vacuolation. Overall, the malignant hepatocellular tumors developed in $p21^{+/Tert}$ and $p21^{+/TertCi}$ mouse models were well-to-moderately differentiated hepatocellular carcinomas with trabecular and/or solid growth patterns. Finally, in humans, the adjacent non-tumor liver will be cirrhotic in 80-90% of HCC cases. In our mouse models, hepatic fibrosis of the adjacent parenchyma was minimal to mild, indicating a notable difference from the human disease and its pathogenesis. It is worth noting that hepatocellular hyperplasia was observed in the liver of a wild-type mouse (designated WT4), and was characterized alongside the liver tumors found in $p21^{+/Tert}$ and $p21^{+/TertCi}$ mice (Figure 1).

To assess tumor cell proliferation, we examined Ki67 expression, a well-established proliferation marker. In human HCC, Ki67 levels are associated with aggressive highly proliferative tumors (Ramos-Santillan *et al*, 2024). Consistent with this, all tumors in our study showed markedly increased Ki67 staining compared to normal liver tissue (Figure 1; (Schaeffer

138 *et al*, 2023)). LT941 exhibited strong Ki67 labeling, reflecting a highly proliferative phenotype
139 whereas LT992 and LT984 both classified as HCA showed minimal Ki67 labeling (Figure 1).
140 All remaining tumors exhibited high Ki67 levels. We also assessed the levels of gH2AX, a
141 marker of DNA double-strand breaks (DSBs) and genomic instability. Elevated DSBs have
142 been reported in neoplastic lesions of HCC (Xiao *et al*, 2014). We observed high gH2AX
143 staining in LT662 and LT941, and in both tumors the extent of 53BP1 labeling paralleled Ki67
144 expression (Figure 1). Elevated gH2AX levels were also detected in LT20-1 and LT20-3, two
145 HCC tumors arising in the same mouse (see below).
146 Together, our results show that aged $p21^{+/Tert}$ and $p21^{+/TertCi}$ mice (>18 months) develop well-
147 differentiated liver tumors, predominantly hepatocellular carcinoma (HCC). The ability of both
148 active and inactive TERT, when expressed under the *p21* promoter, to promote tumor formation
149 suggests that TERT contributes to hepatocarcinogenesis also through telomere independent
150 mechanisms.
151
152 **Distinct somatic mutation profiles in $p21^{+/Tert}$ and $p21^{+/TertCi}$ tumors**
153 We characterized the mutational landscape of liver tumors from aged $p21^{+/Tert}$ and
154 $p21^{+/TertCi}$ mice using Whole Exome Sequencing (WES). This analysis identified coding
155 mutations in driver genes and copy number alteration (CNA) (Table S1 and S2). We examined
156 somatic mutations associated with hepatocellular carcinoma (HCC) in both humans and mice
157 (**Erreur ! Source du renvoi introuvable.**A, Table S1, dataset1) (Kan *et al*, 2013; Zhang *et al*,
158 2014; Totoki *et al*, 2014; Letouzé *et al*, 2017; Connor *et al*, 2018; Chen *et al*, 2024; Lee, 2015).
159 In liver tumors from aged $p21^{+/Tert}$ mice, LT662 and LT663 carried activating mutations in
160 *Ctnnb1*, which encodes β-catenin (*Ctnnb1*^{Asp32Tyr} and *Ctnnb1*^{Thr41Ile}, respectively) (Figure 2A).
161 LT662 also harbored mutations in *Col11a1* (*Glu1155Lys*), present in ~6.8% of human HCCs
162 (Kan et al., 2013), and in the histone demethylase *Kdm4d* (*Gln73His*). LT663 carried mutations
163 in *Kdm3c* (*Arg278Gly*), a demethylase regulating adipogenic transcription factors (Viscarra et
164 al., 2020), and *Ddias* (*Pro706Leu*), a gene linked to DNA damage-induced apoptosis and
165 elevated in HCC (Im *et al*, 2023). Tumor LT992 showed few mutations and no CNAs but
166 contained two frameshift mutations: one in *Ppp1r9a* (*Leu1273Thrfs*), a regulatory subunit of
167 protein phosphatase 1 (PP1), and another in *PtprE* (Protein tyrosine phosphatase receptor type
168 E). LT992 also had a truncating mutation in *Sucla2* (*Gln87del*), a TCA cycle enzyme. LT941
169 harbored a missense mutation in the Furin-like domain of *Egfr* (*Egfr*^{Ser303Tyr}), a region known
170 to harbor MAPK-activating mutations. Mutations at nearby codon 254 in this domain were
171 frequently found in a carcinogen-induced mouse model of liver cancer (Connor *et al*, 2018). It
172 also carried a splice-site mutation in *Ppp1r1a* (another PP1 subunit) and a *Ptpn5* (*Arg246Gly*)
173 mutation, encoding PP5 (Protein Phosphatase 5) (Figure 2A).
174 Strikingly, three of five liver tumors from aged $p21^{+/TertCi}$ mice (LT981, LT20-3, and LT24)
175 harbored the same activating *Hras* mutation (*Hras*^{Gln61Lys}) (Figure 2A) a known hotspot in
176 diethylnitrosamine (DEN)-induced murine liver tumors (Connor *et al*, 2018). LT981 also
177 carried a missense mutation in Rnf43 (*Rnf43*^{Thr208Pro}), an E3 ubiquitin ligase. LT20-3 harbored
178 multiple mutations, including a C-terminal deletion in the histone methyltransferase *Kmt2d*
179 (*Kmt2d*$^{Gln4282del)}$, which mediates H3K4 monomethylation at enhancers (Lee *et al*, 2013), a
180 frameshift mutation in *Fga* (*Fga*^{Ala245fs}), and a missense mutation in Ep300 (*Ep300*^{Ala74Glu}).
181 LT20-1 which arose in the same mouse as LT20-3 harbored the same *Ep300*^{Ala74Glu} mutation

but lacked the *Hras*^{Gln61Lys} mutation (Figure 2A). LT20-1 also carried a mutation in *Ppp1ca* (*Ppp1ca*^{Arg191Trp}), the catalytic PP1 subunit, as well as a frameshift mutation in *Uri1* (*Uri1*^{Ser481fs}), a transcriptional repressor implicated in ROS suppression (Xu *et al*, 2021). LT24, which showed extensive genomic rearrangement (Figure 2B) had a truncating mutation in *Ogg1* (*Ogg1*^{Cys253Ter}), involved in oxidative DNA damage repair (Boiteux & Radicella, 2000). LT984, classified as a hepatocellular adenoma also carried the *Ep300*^{Ala74Glu} mutation, marking as the third tumor with this recurrent mutation. It also harbored a deletion in *Rnf168* (*Rnf168*^{Glu159Del}), a DSB-repair E3 ligase and a missense mutation in *Fn1* (*Fn1*^{Cys335Gly}), which encodes fibronectin (Figure 2A).

Interestingly, mutations in PP1 subunits were identified in multiple tumors, *Ppp1ca* in LT20-1, *Ppp1r9a* in LT992, and *Ppp1r1a* in LT941 (Figure 2A, Table S1), highlighting a potential role of the PP1 pathway dysregulation in HCC development (see discussion).

Shared chromosomal alterations between p21$^{+/Tert}$ and p21$^{+/TertCi}$ tumors mirror human HCC

We analyzed copy number alterations (CNAs) across the different tumors (Figure 2B, Table S2, Fig. EV1). No detectable gains or losses were found in LT992 and LT984 and minimal alterations in LT20-1, and LT20-3 in contrast of all other tumors (Fig. EV1). Recurrent amplifications included a Chr 15 gain in LT662, LT663, LT981, and LT24, a ChrX gain in LT663 and LT941, and a Chr5 gain in LT941 and LT981 (Figure 2B). With respect to chromosomal losses, LT662, LT981, and LT24 showed a loss on Chr 4, often accompanied by a loss on Chr X. A similar pattern of Chr4 and ChrX loss was also detected in the WT liver neoplasm (WT4) (Figure 2B). Interestingly, LT663 showed extensive rearrangement of Chr 14 (Fig. EV1), indicative of chromothripsis, a catastrophic chromosomal shattering and reassembly event previously reported approx. 5% of human HCC cases (Fernandez-Banet *et al*, 2014; Chen *et al*, 2024).

We compiled a curated list of genes recurrently amplified or deleted in human HCC (Zucman-Rossi *et al*, 2015; Schulze *et al*, 2016; Niu *et al*, 2016; Letouzé *et al*, 2017; Yang *et al*, 2023; Chen *et al*, 2024) and found strong parallels in the mouse tumors (Figure 2C). In particular, the conserved amplification on Chr 15 includes several key genes (*Myc, Cthrc1, Rad21, Ndrg1*, and *Ptk2*) linked to liver tumorigenesis, tumor growth, metastasis, or immune evasion (Dhanasekaran *et al*, 2022; Sun *et al*, 2024; Pang *et al*, 2024; Tang *et al*, 2023; Fan *et al*, 2019). Additional amplifications include *Met* in LT663 and *Ccnd1* and *Fgf15* (the murine ortholog of human *FGF19*) in LT24 frequently amplified in human HCC (Schulze *et al*, 2015). Chr 5 gains in LT941 and LT981 includes *Sdhc* and *Parp1*, genes implicated in HCC progression (Bai *et al*, 2022; Paturel *et al*, 2022). Both tumors also showed *Mdm4* amplification, a negative regulator of TP53 found overexpressed in fibrolamellar HCC, particularly in adolescent patients whose tumors often lack TP53 mutations (Karki *et al*, 2019) (Figure 2C). Among genes affected by copy number loss, only LT24 harbors a *Tp53* deletion. *Cdkn2a*, *Cdkn2b*, and *Ard1a* (Chr 4) on their side are deleted in LT662, LT981**,** and LT24 while LT663**,** LT981**,** and LT24 share a deletion of cell cycle regulators *Cdc25* and *Rb1*. Loss of these genes is linked to senescence bypass and liver tumorigenesis (Niu *et al*, 2016; Zucman-Rossi *et al*, 2015; Joseph *et al*, 2019; Reimann *et al*, 2024). LT941 and LT24 also show deletions in alcohol dehydrogenase genes, including *Adh4*, whose loss correlates with poorer HCC prognosis

226 (Zhang *et al*, 2023) (Figure 2C). Unlike human HCC where *TERT* is frequently activated, about
227 half of the tumors exhibited loss of the endogeneous *Tert* locus, likely due to the mouse models
228 used in which *Tert* or *Tert*^{Ci} are expressed under the control of the *p21* promoter, rendering
229 activation of the native locus dispensable.
230 In conclusion, despite the limited sample size, our findings show that both *p21*$^{+/Tert}$ and
231 *p21*$^{+/TertCi}$ mouse models-which mimic telomerase activation in pre-senescent cells-develop
232 HCCs with key molecular and histopathological features of human liver cancer.
233
234 **Activating RAS mutations in p21$^{+/TertCi}$ tumors are associated with elevated mutagenesis**
235 We identified recurrent mutations in *Hras*^{Gln61Lys} (LT981, LT24, LT20-3) and *Ep300*^{Ala74Glu}
236 (LT984, LT20-1, LT20-3) in p21$^{+/TertCi}$ tumors. Notably, in a (DEN)-induced mutagenesis
237 model, half of all liver tumors harbored *Hras* mutations at position Gln61, with Hras^{Gln61Arg}
238 being the most frequent (Connor *et al*, 2018). We examined the number and pattern of mutations
239 observed across tumors (Figure 3A). Among p21$^{+/Tert}$ tumors, LT662, LT663, and LT941
240 exhibited high levels of mutations while LT992 was sparsely mutated (Figure 3A). p21$^{+/TertCi}$
241 Tumors harboring the *Hras*^{Gln61Lys} mutation exhibited the higher number of mutations, whereas
242 the two tumors (LT984 and LT20-1) with the Ep300^{Ala74Glu} displayed a lower mutation burden.
243 Mutational signatures analysis in p21$^{+/Tert}$ and p21$^{+/TertCi}$ tumors revealed that C>A
244 transversions (20% of the mutations) occurred at similar overall frequencies in both tumor types
245 while C>T transitions were slightly more frequent (35% et 45% in *p21*$^{+/Tert}$ and *p21*$^{+/TertCi}$
246 tumors, respectively) (Figure 3B). C>T transitions occurred preferentially in similar contexts
247 A[C>T]G and C[C>T]G in both type of tumors (Figure 3C). Interestingly, in p21$^{+/Tert}$ tumors
248 C>A transversions predominantly occurred in A[C>A]T and T[C>A]T contexts whereas in
249 p21$^{+/TertCi}$ tumors they were mainly enriched in G[C>A]A and T[C>A]T contexts (Figure 3C).
250 The oncogenic mutations Egfr^{Ser303Tyr} (TCA /TAT) and Ep300^{Ala74glu} (GCA/GAA) arose in such
251 context. At the individual tumor level C>A transversions were enriched in LT941, LT981,
252 LT24, and LT203, all harboring activating RAS mutations (Figure 3D). Oddly LT992 showed
253 no evidence of mutagenesis apart from a few isolated T>G. The few mutations in LT992 are in
254 frame deletions or frameshift variant.
255 The mutagenic effect associated with the expression of TERT and TERT^{Ci} and their subsequent
256 amplification though the emergence of oncogenic mutations are addressed in the discussion.
257
258 **Oncogenic signalling pathways in p21$^{+/Tert}$ and p21$^{+/TertCi}$ tumors**
259 We performed RNA-seq analysis on nine liver tumors, including four from p21$^{+/Tert}$ mice, five
260 from p21$^{+/TertCi}$ mice, one neoplasm from a wild-type (WT) mouse, and six healthy liver samples
261 collected from tumor-bearing mice. Principal Component Analysis (PCA) revealed a separation
262 between healthy and tumor samples based on their global gene expression profiles (Fig. EV2A),
263 highlighting the distinct transcriptional landscape of the tumors. We identified differentially
264 expressed genes (DEGs) between tumor and healthy liver tissues (Table S3). We found that
265 many of the significantly up- and down-regulated genes were also deregulated in HCCs from
266 the *Axin1*Δ mouse model (Abitbol *et al*, 2018) (Fig. EV2B) and in human HCC, underscoring
267 the biological relevance of our models and the presence of conserved HCC markers across
268 species.

We next analyzed the 200 most differentially expressed genes in either p21$^{+/Tert}$ or p21$^{+/TertCi}$ tumors compared to non-tumoral liver tissues (Figure 4A). Among these, 45 and 25 genes were commonly upregulated or down regulated, respectively, in both tumor types. 155 genes were selectively overexpressed in either p21$^{+/Tert}$ or p21$^{+/TertCi}$ tumors whereas 175 genes were down-regulated. Gene Ontology analysis of Biological Processes (GOBP) associated with the upregulated genes revealed distinct patterns between the two models. In p21$^{+/Tert}$ tumors, enriched pathways were primarily related to sister chromatid segregation and mitosis (Figure 4B). In contrast, p21$^{+/TertCi}$ tumors showed a significant upregulation of genes involved in wound healing, angiogenesis, and the ERK1/ERK2 signaling cascade, aligning with the presence of the *Hras*^{Gln61Lys} mutation in three of the five tumors. Consistent with these findings, p21$^{+/Tert}$ tumors overexpress cyclin-dependent kinase 1 (Cdk1) and Cdk6, along with multiple cyclins (Ccna2, Ccnb1, Ccnb2, Ccnd1), in contrast to p21$^{+/TertCi}$ tumors for which such upregulation is in most case not significant (Figure 4C).

We next sought to identify transcriptional signatures indicative of signaling pathway activation, specifically Wnt/β-catenin, ERK1/ERK2 (MAPK), Notch, and Sonic Hedgehog (SHH), all of which are frequently implicated in human HCC (Zucman-Rossi *et al*, 2015). As expected from their mutational profiles (*Ctnnb1*^{Asp32Tyr} and *Ctnnb1*^{Thr41Ile}), LT662 and LT663 displayed strong activation of the Wnt/β-catenin pathway (Figure 4D). These two tumors showed high expression of a ten-gene mutated β-catenin gene signature comprising AXIN2, GLUL, LGR5, NKD1, NOTUM, RHBG, SLC13A3, SP5, TCF7, and TNFRSF19 which has been reported to identify CTNNB1-mutated HCC (Lehrich *et al*, 2024). In addition, LT662 and LT663 showed marked overexpression of the Na^+-dependent amino acid transporters SLC1A5, which mediates glutamine uptake and has recently been recognized as a novel hallmark of HCC (Tambay *et al*, 2024), and SLC1A2, which transports glutamate.

Tumors harboring the *Hras*^{Gln61Lys} mutation, LT24, LT20-3, and LT981 (all from p21$^{+/TertCi}$ mice), along with LT941 (p21$^{+/Tert}$, carrying Egfr^{Ser306Tyr}) exhibited a shared transcriptional signature consistent with ERK1/ERK2 (MAPK) pathway activation, in alignment with their mutational backgrounds (Figure 4E). Further, LT662, LT663, and LT992 exhibited transcriptional features of Notch pathway activation, similar to those observed in *Axin*Δ mouse models (Villanueva *et al*, 2012; Abitbol *et al*, 2018) (Figure 4F). A distinct Sonic Hedgehog (SHH) signature was found in LT981, LT984, LT992, and LT24 (Figure 4G), indicating additional heterogeneity in pathway activation across tumors. Overall, the transcriptomic profiles of the tumors are largely consistent with their underlying mutational landscapes. Interestingly, LT992 showed a MAPK activation signature, despite lacking canonical *RAS* pathway mutations. We hypothesize that this activation could result from mutations in phosphatase genes (PtprE and Ppp1r9a), which may lead to increased substrate phosphorylation and thereby activate MAPK signaling (Chen *et al*, 2024).

Among model-specific transcriptional signatures, only p21$^{+/Tert}$ tumors exhibited overexpression of the helicase Pif1 and Ten1, a component of the CST complex (Ctc1/Stn1/Ten1) involved in telomere replication and stability (Wang *et al*, 2012) (Fig. EV3A). Additionally, nearly all tumors, except LT984 and LT20-1, showed strong overexpression of the maternally imprinted long noncoding RNA *H19* and its associated microRNA, miR-675, both of which have been implicated in liver cancer pathogenesis (Wang *et al*, 2023) (Fig. EV3B).

313 **Tumors exhibit suppressed gluconeogenesis but upregulate distinct Nfrf2 target genes**
314 A recent study (Gu *et al*, 2025) showed that during the progression from metabolic dysfunction–
315 associated steatohepatitis (MASH) to HCC, FBP1 expression declines in premalignant
316 hepatocytes. To explore metabolic alterations in the tumor samples, we analyze the expression
317 of genes involved in glycolysis and gluconeogenesis. Enzymes involved in gluconeogenesis
318 Aldob, Fbp1, Pcx, Pck1, and G6pc (Group 1) were consistently downregulated across all
319 tumors, except for LT984 (Figure 5A). Conversely, glycolytic enzymes (Group 2) were
320 generally overexpressed in all tumors again with LT984 as the exception. In particular, Hk2,
321 Eno1, Tpi1, and Gapdh (Group 3) were strongly upregulated in tumors LT662, LT663, LT201,
322 and LT203 (Figure 5A). These findings indicate that, apart from LT984 (HCA), all tumors
323 suppress gluconeogenesis in favor of enhanced glycolytic activity (Figure 5A). In particular,
324 Fbp1 was downregulated in all tumor samples except LT984 (Figure 5B). Because Fbp1 down
325 regulation was associated to NRF2 activation (Gu *et al*, 2025), we examine the expression of
326 Nrf2 (Nfe2l2) target genes (Malhotra *et al*, 2010; Mitsuishi *et al*, 2012b). We found that most
327 Nrf2 targets involved in redox and energy metabolism regulation (Luchkova *et al*, 2024) were
328 differentially regulated in tumor samples (Figure 5C). Interestingly, $p21^{+/Tert}$ and $p21^{+/TertCi}$
329 tumors exhibited distinct Nrf2 target expression patterns based on their mutational profiles
330 (Figure 5C). For instance, LT662 and LT663, which harbor activating mutations in Ctnnb1,
331 preferentially upregulated a subset of Nrf2 targets (Group 1) including Tkt (transketolase) and
332 Taldo1 (transaldolase 1) involved in the pentose phosphatase pathway, core regulator of
333 glutathione synthesis and antioxidant defence (Gclm, Sqstm1, Mafg), as well as Nupr1, a stress
334 responsive gene induced under oxidative and metabolic stress and known to be expressed in
335 human HCC (Huang *et al*, 2021; Cai *et al*, 2025) (Figure 5C). In contrast, tumors LT941,
336 LT992, LT24, LT201, LT203, and LT981 predominantly upregulated genes involved in
337 antioxidant defense (Group 2) including Slc7a11, Gpx4, Nqo1, Txnrd1, Fth1, Hmox1, and Gsr,
338 all being regulators of ferroptosis resistance, a cell death pathway driven by lipid peroxidation
339 (Koppula *et al*, 2021; Su *et al*, 2025) (Figure 5C). When considering all tumors, neither Nrf2
340 nor Tp53 are significantly overexpressed in tumors (Fig. EV3C). Notably, although Nrf2
341 mRNA levels were higher in LT992 and LT24 compared to LT203 and LT981, the latter two
342 showed the strongest upregulation of Nrf2 target genes. This suggests that Nrf2 protein
343 stabilization may drive its activity in the tumors rather than its transcriptional regulation.
344
345 **Spatial analysis reveals altered HNF4alpha protein levels and liver tissue architecture**
346 We employed the Hyperion™ Imaging System, which enables high-dimensional, subcellular-
347 resolution analysis of multiple cellular targets simultaneously in formalin-fixed paraffin-
348 embedded (FFPE) tissues (Elaldi *et al*, 2021). Using a validated panel of 10 metal-conjugated
349 antibodies (Table S4), we analyzed the architecture of the tissues. To characterize the liver
350 parenchyma, we first stained healthy livers and the tumors from $p21^{+/Tert}$ and $p21^{+/TertCi}$ mice
351 using antibodies directed against beta-catenin (Ctnnb1), Hepatocyte nuclear factor 4α
352 (HNF4alpha), and alpha Smooth Muscle Actin (α-Sma) (Figure 6A, B). Scale bars (200 µm)
353 corresponding to the uncropped images are provided in Fig. EV4. In healthy $p21^{+/Tert}$ (L1069)
354 and $p21^{+/TertCi}$ (L982) livers (Figure 6A), a majority of cells were stained by HNF4alpha
355 antibodies likely marking non-transformed hepatocytes. Beta-catenin displayed a typical wild-
356 type distribution with predominant localization at hepatocyte plasma membrane consistent with

357 its role in cell-cell adhesion and α-SMA was primarily restricted to the perivascular regions
358 where smooth muscle cells reside (Figure 6A). It was challenging to distinguish whether 4T1
359 or LT662 and LT663 tumors, which share an activating mutation in Ctnnb1, exhibited higher
360 levels of cytoplasmic or nuclear beta-catenin indicative of beta-catenin activation (Figure 6A).
361 Notably, all tumors, showed a reduced number of HNF4alpha-positive cells as well as a
362 decrease in staining intensity (see the following paragraph for HNF4alpha quantification across
363 tumors). Moreover, unlike the perivascular localization observed in the healthy livers, we
364 observed dispersed α-Sma positive cells throughout the tumor likely reflecting the presence of
365 cancer associated fibroblasts (Sun *et al*, 2023; Xu *et al*, 2022). In tumors LT941, LT992, and
366 LT201, α-Sma positive areas accounted for more than 20% of the area occupied by DNA,
367 indicating an important stromal activation.
368 We next quantified HNF4alpha and also p21 positive cells across all the samples (Figure
369 7A, B). In healthy $p21^{+/Tert}$ and $p21^{+/TertCi}$ livers 40 to 50% of liver cells expressed HNF4alpha.
370 This proportion dropped sharply to 10% or less in the tumors harboring the $Ctnnb1^{Asp32Tyr}$,
371 $Ctnnb1^{Thr41Ile}$, $Egfr^{Ser303Tyr}$, and $Hras^{Gln61Lys}$ mutations (Figure 7A, B). In contrast, tumors
372 lacking activation of the Wnt/β-catenin or hRAS signaling pathways retained approximately
373 20% of HNF4alpha-positive cells (Figure 7A, B). Reflecting hepatocyte dedifferentiation,
374 tumors exhibited strong downregulation of major urinary protein genes, normally produced by
375 hepatocytes in mice (Fig. EV5A) (Krauter *et al*, 1982).
376 These findings prompted us to examine the transcript levels of HNF4alpha. RNA-seq
377 analysis did not reveal significant downregulation of Hnf4alpha mRNA levels across tumor
378 samples (Table S3) suggesting that HNF4alpha may be subject to post-transcriptional
379 regulation in tumors with an activation of the Wnt/β-catenin or hRAS signaling.
380 On the same FFPE sections, we quantified the proportion of p21-positive cells. In L1069
381 ($p21^{+/Tert}$) and 4T1 ($p21^{+/+}$) livers, fewer than 2% of cells were p21-positive compared to
382 approximately 5 % in L982 healthy liver ($p21^{+/TertCi}$) (Figure 7A, B). This proportion increased
383 to above 10% in LT941, LT992, LT984, and LT201 (Figure 7A, B) and was about 5% for the
384 other tumors consistent with the transcriptional overexpression of p21 in all tumors (Table S3).
385 One tumor (HCA), LT992, exhibited a markedly higher proportion of p21-positive cells (>20%)
386 (Table S3). Interestingly, in LT992 and LT984 both classified as hepatocellular adenoma
387 (Figure 1, Table 1), approximately 50 % of HNF4alpha-positive cells were also positive for
388 p21. Notably, both tumors display high levels of TERT mRNA, suggesting that TERT may
389 drive hepatocyte proliferation in these two tumors which lack mutations in the Wnt/β-catenin
390 and hRAS pathways.
391
392 **Tumor infiltration by immune cells is altered in β-catenin–activated HCC**
393 We further assessed immune cell infiltration within the tumors. To characterize the infiltration
394 of lymphocyte classes, we used metal-conjugated antibodies against CD3 (T lymphocytes),
395 CD4 (auxiliary T lymphocytes), CD8 (cytotoxic T lymphocytes), and B220 (B lymphocytes).
396 We found that the two beta-catenin activated tumors (LT662 and LT663) were poorly infiltrated
397 by T-lymphocytes (2 to 4 % of CD3-postive cells) with 1-2% of auxiliary and cytotoxic T
398 lymphocytes (Figure 8A, B). These results are consistent with previous studies showing that
399 activation of the Wnt/β-catenin pathway in HCC is associated with poor T-lymphocyte
400 infiltration, facilitating immune evasion and resistance to anti-PD1 therapy (Dantzer *et al*,

2024). In contrast, LT992, LT201, and LT941 tumor showed higher level of T lymphocyte infiltration (> 10 %) (Figure 8A, B). While LT201 was characterized by a higher proportion of auxiliary ($CD4^+$) T cells (8-10 %) compared to cytotoxic ($CD8^+$) T cells (<4%), the highly aggressive LT941($Egfr^{Ser303Tyr}$) displayed a predominance of cytotoxic T cells (approx.10%) over auxiliary T cells (Figure 8A,B). LT981, LT203, and LT24 tumors, all carrying the $Hras^{Gln161Lys}$ mutation, displayed comparable intermediate levels of lymphocyte infiltration (approx.5%). In summary, the two β-catenin–activated tumors exhibited the lowest levels of T-cell infiltration, whereas the Egfr-activated tumor along with tumors LT992 and LT201 (which both harbor mutations in subunits of PPP1 exhibited the highest degree of T lymphocyte infiltration (approx. 5%). Regarding B lymphocyte infiltration, tumors exhibited very low levels of infiltrating B lymphocytes (1 to 3%) (Figure 8A, B). Only LT981 exhibited a proportion of infiltrating B lymphocytes exceeding 5%.

We further quantified the proportion of macrophages (F4/80) and dendritic cells (Cd11c) in the liver samples (Figure 9A, C). In healthy liver samples (L1069 and L982), F4/80 positive-cells accounted for approximatively 15% of total liver cells likely, consistent with their identification as kupffer cells (Figure 9A, C). This proportion increase to about 25% in the 4T1 neoplastic tissue carrying the $Ctnnb1^{Se45Phe}$ but not the activated beta-catenin signature. The percentage of macrophages in tumors ranged from 5% in minimally infiltrated tumors (LT662 $Ctnnb1^{Asp32Tyr}$, LT663 $Ctnnb1^{Thr41Ile}$, LT984 $Ep300^{Ala74Glu}$) to 20-25% in highly infiltrated tumors (LT941 $Egfr^{Ser303Tyr}$, LT981 $Hras^{Gln61Lys}$, LT203 $Hras^{Gln61Lys}$), suggesting that the degree of macrophage infiltration is associated with the oncogenic driver and reflects heterogeneity within the tumor microenvironment (TME). Among these macrophages, in both healthy and tumor tissue of aged $p21^{+/Tert}$ and $p21^{+/TertCi}$ mice, only 2 to 5% were positive for p21indicating that the vast majority of macrophages do not express p21 (Figure 9B, C). Dendritic cells (Cd11c) infiltration was low in healthy livers (1-2%) and in LT662 and LT663 tumors, which show generally weak immune cell infiltration as well as in LT984 (HCA) (Figure 9A, C). LT992, LT24, and LT201 showed higher levels of dendritic cell infiltration with marked punctuate staining (Figure 9C). Interestingly, tumors such as LT941 and LT203 tumors, being markedly infiltrated by macrophages (>20%), exhibited low levels of dendritic cells (3 to 7 %) suggesting competitive dynamics between macrophages and dendritic cells in the TME.

Discussion

The $p21^{+/Tert}$ and $p21^{+/TertCi}$ mouse models develop hepatocellular liver tumors, including hepatocellular carcinomas (HCC) and hepatocellular adenomas (HCA). In our murine models, HCCs resemble human HCCs in many histomorphological aspects, including trabecular and solid growth patterns, multifocal necrosis, hemorrhage, and well- to moderately differentiated tumor cells with mild to moderate atypia. These features support the translational relevance of these models for studying human HCC. However, a notable difference lies in the condition of the adjacent non-tumoral liver: while human HCCs typically arise in a cirrhotic liver background (in 80–90% of cases), the surrounding parenchyma in these murine models exhibits only minimal to mild fibrosis and non-significant liver damage, indicating a divergence in the underlying liver pathology and disease context. It is important to note that by 9 months of age, male $p21^{+/Tert}$ and $p21^{+/TertCi}$ mice developed obesity accompanied by hepatic steatosis, which was associated with altered feeding behavior (L. Braud and V. Géli, unpublished results), suggesting a link between early metabolic dysfunction and later tumor development.

The finding that conditional expression $TERT^{Ci}$ promotes liver tumorigenesis in aged mice raises questions about the mechanism through which $TERT^{Ci}$ drives tumor development. Since models $p21^{+/Tert}$ and $p21^{+/TertCi}$ retain an intact endogenous *Tert* locus, the possibility of endogenous Tert reactivation was considered. However, no mutations were found in the *Tert* promoter region, and CNA analysis suggest a loss rather than amplification of *Tert* locus (Figure 2C). We rather favor the possibility is that $TERT^{Ci}$ modulates a signaling pathway that promotes liver tumor development. This analysis is complex as most tumors are also associated with oncogenic mutations. Comparison of transcriptional profiles between healthy control and $p21^{+/Tert}$ or $p21^{+/TertCi}$ livers from 18-month-old mice reveals that the proto-oncogenes Fos and Jun are overexpressed mainly in $p21^{+/TertCi}$ healthy livers from aged mice, suggesting that $p21^{+/TertCi}$ livers may be in a pro-tumorigenic state that could promote the occurrence of HCC (Bakiri *et al*, 2017, 2024). Another possibility is that $TERT^{Ci}$ exerts a protective capping function at chromosome ends that does not rely on telomere elongation. Supporting this hypothesis, Tpp1 which recruits TERT a chromosome ends (Zhong *et al*, 2012) is expressed across all tumors. Finally, it is also possible that a mitochondrial form of $TERT^{Ci}$ (and TERT) contributes to tumor development by safeguarding mitochondrial DNA and function (Haendeler Judith *et al*, 2009; Saretzki, 2014) in tumors that are exposed to high oxidative stress. This hypothesis is consistent with the observed overexpression of Src in all tumors, as Src kinase activity has been shown to promote the nuclear export of TERT (Haendeler *et al*, 2003). At another level, Pif1 and Ten1 involved in telomere replication and processing (Snow *et al*, 2007; Feng *et al*, 2018; Sanz-Moreno *et al*, 2025) were overexpressed only in $p21^{+/Tert}$ tumors. PIF1 was identified in a study as one of nine prognostic mRNAs in human hepatocellular carcinoma (HCC) (Ni *et al*, 2020) suggesting that overexpression of PIF1 is associated with TERT reactivation.

We observed that $p21^{+/Tert}$ tumors were associated with distinct oncogenic mutations. Specifically, the $Ctnnb1^{Asp32Tyr}$ and $Ctnnb1^{Thr41Ile}$ variants are both well-characterized exon 3 gain-of-function mutations known to activate Wnt/β-catenin signaling (Rebouissou *et al*, 2016; Dantzer *et al*, 2024). Consistent with this, LT662 and LT663 displayed a strong transcriptional signature of β-catenin activation (Figure 4D). In addition to β-catenin mutations, LT662 and LT663 carried mutations in Kdm4d (Jmjd2d) and Kdm3c, respectively, two distinct JmjC H3K9

478 demethylases. Notably, KDM4D has been reported to physically interact with β-catenin and to
479 demethylate H3K9me3 at promoters of β-catenin target genes in colorectal cancer cell lines
480 (Peng et al., 2019). This raises the intriguing question of whether the Kdm4d^{Gln73His} mutation
481 observed in LT662 might impact β-catenin–driven transcription in this context. Notably,
482 mutations *Kdm4d* and *Kdm3c* were exclusive to LT662 and LT663, suggesting potential roles
483 in Wnt pathway modulation. Surprisingly, LT992 exhibited no genomic rearrangements but did
484 harbor two frameshift mutations in the phosphatases *Ppp1r9a* and *PtprE*. Similar mutations
485 were observed in multiple tumors in this study (Figure 2A, Table S1). Of note, recent work has
486 reported mutations in UTR regions of PP1 subunits in human HCC (Chen *et al*, 2024). At the
487 transcriptional level, LT992 displays a distinct signature shared with LT662 and LT663 tumors
488 but distinct to the beta-catenin activated signature that, in both humans and mice, is associated
489 with *AXIN1* mutations (Abitbol *et al*, 2018). PP1 has been shown in human cells to bind AXIN
490 and oppose its phosphorylation (Luo *et al*, 2007). We observed suppressed Wnt signaling in
491 LT992 (Fig. 4D), consistent with the expected effect of PP1 inactivation, which likely increases
492 AXIN1 phosphorylation, enhances GSK3-mediated β-catenin degradation, and thereby
493 dampens Wnt pathway activity (Luo *et al*, 2007). This raises the question of what mechanism
494 drives the shared transcriptional signature observed in both Axin1-mutated HCCs and tumors
495 LT662 (Ctnnb1^{Asp32Tyr}), LT663 (Ctnnb1^{Thr41Ile}), and LT992 (Ppp1r9a^{Leu1273Thrfs}) (Fig. 4F).
496 LT992 also carried a truncating mutation in *Sucla2* (Gln87del), previously linked to succinyl-
497 CoA accumulation and protein hypersuccinylation. Elevated protein succinylation has been
498 observed in HCC tissues compared to adjacent normal liver and may be associated with poor
499 prognosis (Bai *et al*, 2022), although its direct role in hepatocarcinogenesis remains uncertain.
500 LT941 also harbored a splice-site variant in another PP1 regulatory subunit, *Ppp1r1a*, along
501 with a mutation in *Ptpn5* (Arg246Gly), which encodes protein phosphatase 5 (PP5). PP5
502 inhibition has been shown to suppress HCC growth by activating AMPK signaling (Chen *et al*,
503 2017). Interestingly, LT941 also exhibited the AXIN1-associated transcriptional signature,
504 further reinforcing the connection between phosphatase subunit mutations and AXIN1-related
505 pathway dysregulation. These findings underscore the significant potential role of phosphatases
506 in liver cancer development.
507 Surprisingly, three of five tumors from aged p21$^{+/TertCi}$ mice (LT981, LT20-3, LT24) shared
508 the activating *Hras*^{Gln61Lys} mutation. Gln61 is a mutation hotspot (*Gln61Lys*, *Gln61Arg*,
509 *Gln61Leu*) found at high frequency in DEN-induced liver tumors, but absent in spontaneous
510 cases (Connor *et al*, 2018). LT981, LT20-3, LT24 displayed the highest level of mutagenesis.
511 The finding that tumors harboring activating RAS mutations exhibit increased mutagenesis was
512 notably evident in the comparison between LT20-1 and LT20-3 which originate from the same
513 liver and are genetically similar except for the presence of *Hras*^{Gln61Lys} in LT20-3. Of note, the
514 Hras^{Gln61Lys} (CAA/AAA) arose from a C>A transversion. In the DEN-induced mouse model,
515 T>A and T>C predominate reflecting the mutagenic properties of DEN (Connor *et al*, 2018).
516 In contrast, tumors from the p21$^{+/Tert}$ and p21$^{+/TertCi}$ mice show a higher frequency of C>A and
517 C>T mutations. The predominance of C>T transitions in ACG and CCG contexts (Fig. 3e)
518 suggests that the enrichment of C>T mutations in both tumor types may reflect proliferation-
519 associated cytosine deamination likely at CpG dinucleotides (Alexandrov *et al*, 2020; Tate *et*
520 *al*, 2019) although LT941 (Egfr^{Ser303Tyr}) despite being is the most highly proliferative tumor did
521 not exhibit higher overall mutational burden compared with *Hras*^{Gln61Lys}mutated tumors (Fig.

522 3a). On their side, C>A transversions are often linked to oxidative DNA damage. Notably, these
523 transversion occurred predominantly in distinct trinucleotide context (ACT and GCA in $p21^{+/Tert}$
524 and $p21^{+/TertCi}$ mice, respectively), both contexts being consistent with oxidative stress, but the
525 difference may be linked to the associated oncogenic mutation reflecting mechanistic difference
526 in tumor initiation and evolution in these models. Interestingly, LT24 which exhibits the highest
527 mutational burden and mutations across multiple nucleotides carries a truncating in
528 $Ogg1^{Cys253Ter}$ mutation. The results raise the question of whether $TERT^{Ci}$ expression contributes
529 to the emergence of the $Hras^{Gln61Lys}$ (CAA/AAA) mutation through a direct or indirect specific
530 mutagenic effect, or whether it instead reflects enhanced cell survival and proliferation. In our
531 previous work, we found that TERT, but not $TERT^{Ci}$, reduces oxidative damage (Lipskaia *et*
532 *al*, 2024; Braud *et al*, 2025). The high mutation burden in *Hras*-driven tumors might be a
533 consequence of the oncogene's own mutagenic activity. Similarly, LT984, LT20-1, and LT20-
534 3 all harbor the same *Ep300* mutation (Ala74Glu; GCA→GAA), which also arises from a C>A
535 transversion. *EP300* mutations are present in only 2% of hepatocellular carcinoma (HCC) cases
536 in the TCGA Pan-Cancer Atlas cohort (n = 366, whole-exome sequenced). The functional
537 significance of the Ala74Glu variant remains unknown. As mentioned in the results LT20-1
538 harbors a mutation in Ppp1ca while LT20-3 harbors a mutation in Kmt2d. *KMT2D* is one of the
539 genes frequently disrupted by hepatitis B virus (HBV) integration in human HCC (Sung *et al*,
540 2012), and mutations are commonly seen in DEN-induced HCC (Connor *et al*, 2018). $p21^{+/TertCi}$
541 harbors several additional mutations. Notably, LT981 and LT984 carry mutations in two
542 distinct E3 ubiquitin ligases: *Rnf43* and *Rnf18*, respectively. *RNF43* mutations are frequently
543 observed in colorectal and gastric cancers (Giannakis *et al*, 2014; Wang *et al*, 2014), and have
544 been associated with poor prognosis in liver cancer (Belenguer *et al*, 2022). *RNF168* targets the
545 histone demethylase KDM4A which specifically demethylates H3K9me3 and H3K36me3, for
546 proteasomal degradation (Mallette *et al*, 2012). Loss of *RNF18* may therefore lead to KDM4A
547 stabilization, potentially altering histone methylation dynamics and epigenetic regulation. In
548 addition, LT984 harbored a mutation in *Fn1* ($Fn1^{Cys335Gly}$), encoding fibronectin. *FN1* is often
549 affected by HBV integration in non-tumor liver tissues adjacent to HCC (Sung *et al*, 2012) but
550 its direct role in tumorigenesis remains unclear.
551 Although $p21^{+/Tert}$ and $p21^{+/TertCi}$ have distinct mutations in oncogenic drivers, they exhibit
552 similar patterns of copy number alterations. For example, LT662 and LT663 share
553 amplifications in Chr15 with LT981 and LT24, which are associated with tumor development.
554 However, these four tumors display distinctly different transcriptional profiles, suggesting that
555 oncogenic mutations play a major role in shaping their transcriptional landscapes. Notably,
556 LT992, LT20-1, and LT20-3 exhibit no or little CNA, reinforcing the idea that driver mutations
557 primarily shape transcriptional patterns. Interestingly, half of the HCCs exhibit deletions in
558 various genes involved in cell cycle regulation, including *Cdkn2a*, *Tp53*, and *Rb1*. Loss of these
559 genes are likely to facilitate the bypass of cellular senescence.
560 Transcriptomic analysis reveals that all tumors except LT984, identified as a hepatocellular
561 adenoma, exhibit downregulation of *Fbp1*. This reduction has been associated with activation
562 AKT and NRF2 pathways, along with decreased expression of p53 and p21, collectively
563 facilitating the bypass of cellular senescence and accumulation of somatic mutations in
564 transformed hepatocytes (Gu *et al*, 2023, 2025). Consistent with these findings, we observed
565 overexpression of *Nrf2* target genes in both $p21^{+/Tert}$ and $p21^{+/TertCi}$ tumors. However, this

566 upregulation did not correlate with *Nrf2* mRNA levels, suggesting that stabilization of the NRF2
567 protein, rather than increased transcription, may underlie the activation of its targets (Zhu *et al*,
568 2025). Importantly, LT662 and LT663, which harbor activating mutations in *Ctnnb1*, display a
569 distinct pattern of *Nrf2* target gene upregulation. These upregulated genes are involved in
570 NADPH generation, red-ox regulation, and oncogene-induced stress such as Nupr1. The NRF2
571 signature in HRAS-mutated tumors exhibits greater heterogeneity, indicating more complex
572 activation of the pathway. Overexpressed genes include NRF2 targets involved in glutathione
573 biosynthesis, reactive oxygen species (ROS) detoxification, and ferroptosis resistance including
574 Slc7a11, features consistent with the increased oxidative stress specific to RAS-induced tumors.
575 It has recently been shown that SLC7A11 is significantly overexpressed in hepatocellular
576 carcinoma (HCC) and that its high expression correlates with lower overall survival, thus
577 highlighting its prognostic value (Zhang *et al*, 2025). Pan-cancer analysis revealed that elevated
578 SLC7A11 associates with higher tumor mutation burden and immunosuppressive
579 microenvironment features (Zhang *et al*, 2025).
580 Spatial characterization of tumors shows that HNF4alpha levels are greatly reduced in HCC
581 with activation of the beta-catenin and hRAS pathways. HNF4alpha is a central regulator of
582 liver function and acts as a tumor suppressor in HCC (Kotulkar *et al*, 2024). It plays a pivotal
583 role in hepatic glucose metabolism (Shokouhian *et al*, 2023) and contributes to the maintenance
584 of hepatocyte quiescence, in part by repressing *cyclin D1* (Ccnd1) expression (Wu *et al*, 2020).
585 Consistently, Ccnd1 was markedly overexpressed in the tumors. In line with findings that
586 identify HNF4alpha as a key regulator of the transition from slow-growing tumors to aggressive
587 HCC (Lazarevich *et al*, 2010), 4T1, LT992 (HCA), and LT984 (HCA) cell lines exhibited
588 intermediate levels of *Hnf4alpha* expression. Surprisingly, we observed that HNF4 alpha levels
589 were downregulated at the post-transcriptional level. In human colon cancer, phosphorylation
590 of HNF4alpha by Src tyrosine kinase has been associated with the loss of specific isoforms of
591 HNF4alpha (Chellappa *et al*, 2012). Degradation of HNF4alpha was further confirmed in liver
592 (Huck *et al*, 2019). As noted above, Src was upregulated in all tumors, albeit to a lesser extent
593 in LT662 raising the possibility that kinases, such as Src may promote HNF4alpha degradation
594 in these tumors.
595 We next analyzed immune cell infiltration in two distinct regions of the tumor. Despite the
596 small size of these regions (1-2 mm^2), the analysis revealed comparable patterns of immune
597 infiltration across both areas of the tumors. Constitutive activation of β-catenin has been shown
598 to suppress immune cell recruitment (Lehrich & Monga, 2025). Approximately 70% of
599 WNT/β-catenin–active tumors are classified as immune-excluded, characterized by low T-cell
600 infiltration (Montironi *et al*, 2023). It has been shown that the immune evasion associated with
601 beta-catenin activation observed in both murine and human HCC results from impaired
602 dendritic cell recruitment (Ruiz de Galarreta *et al*, 2019). Consistent with these findings, LT662
603 and LT663, which exhibit high expression of AXIN2 and GLUL, exhibited low infiltration by
604 T lymphocytes as well as by macrophages and dendritic cells. Chemokines known to attract T-
605 lymphocytes (Ccl2, Ccl5, Ccl17, Ccl22, Cxcl9, Cxcl10, and Cxcl11) showed variable levels of
606 expression across all tumors and their levels could not explain the reduced T lymphocyte
607 infiltration in LT662 and LT663. Only Cxcl12 was consistently down-regulated in these two
608 tumors as well as in several other HCC. The observed immune exclusion may therefore reflect,
609 at least in part, tumor-specific adaptations in metabolic reprogramming and oxidative defense.

Interestingly, Glul-overexpressing tumors LT662 and LT663 specifically exhibited a ~20-fold and a ~10-fold upregulation of *Slc1a5*, whose gene product transports glutamine into cancer cells (Bhutia *et al*, 2015) and of the glutamate transporter *Slc1a2,* respectively. We predict that LT662 and LT663 establish a glutamine- and glutamate-depleted tumor microenvironment by combining high-affinity uptake transporters (SLC1A2, SLC1A5) with intrinsic glutamine synthesis (GLUL), thereby achieving metabolic autonomy while starving immune and stromal cells of critical nitrogen sources. Recently, glutamine was shown to function as a metabolite regulating the cross-talk between tumors and conventional type 1 dendritic cells (cDC1s), thereby licensing cDC1s to activate cytotoxic T cells (Guo *et al*, 2023). It may therefore that tumor evasion in LT662 and LT663 results from reduced glutamine in the TME (Fig. EV5B). The elevated intracellular glutamine concentration may also promote increased glutathione production and strengthen antioxidant defences. Whether this principle extends to human β-catenin–activated tumors remains to be determined. Recent analyses in human HCC revealed that SLC1A5 expression was associated with poor prognosis and an immunosuppressive microenvironment providing a marker to predict immunotherapy response (Zhang *et al*, 2024a, 2024b). hRAS-activated tumors on their side exhibit preferential upregulation of SLC7A11 that imports cystine in exchange for glutamate to support antioxidant defense and protection against ferroptosis (Li *et al*, 2024).

640 # Materials and Methods
641
642 **Animals**
643 Wild-type (C57BL/6J N), p21$^{+/Tert}$, and p21$^{+/TertCi}$ mice were housed under controlled
644 environmental conditions: temperature (21 ± 1 °C), humidity (60 ± 10%), and a 12-hour
645 light/dark cycle. Animals were fed a standard diet (A04, SAFE Diet, Augy, France). All
646 procedures were conducted in accordance with institutional animal care guidelines and were
647 approved by the Institutional Ethics Committee No. 16, Paris, France (license number 16-090).
648 Throughout the study, mice underwent regular assessments including body weight monitoring
649 and metabolic evaluations. Mice were euthanized at over 18 months of age, regardless of the
650 presence or absence of tumor-related signs. Liver tissues were collected and processed for
651 subsequent analyses.
652
653 **Histologic characterization of tumors**
654 Freshly collected mouse liver tissues were fixed in 10% neutral buffered formalin for 24–48
655 hours (fixative:tissue volume ratio of 10:1), transferred to 70% ethanol for 24 hours before
656 paraffin embedding. Paraffin blocks were cut into 5-µm-thick sections, which were
657 subsequently dried overnight at 37 °C and stained with Haematoxylin-Eosin-Saffron (HES)
658 using an automated slide stainer before digitalization. The description and diagnosis of
659 neoplastic and non-neoplastic mouse liver lesions followed the International Harmonization of
660 Nomenclature and Diagnostic Criteria (INHAND) guidelines for Lesions of the Rat and Mouse
661 Hepatobiliary System and the accepted consensual terminology used in mouse pathology, as
662 published by international committees and experts (Thoolen *et al*, 2010; Deschl *et al*, 2001).
663 The researcher performing the histological evaluation (P.C.) was not blinded to sample identity
664 at the time of the analysis. Liver neoplasms were evaluated for tumor architecture and
665 relationship with adjacent tissue, growth pattern, areas of necrosis, neoplastic cell morphology,
666 cytonuclear atypia, stromal composition, and leukocyte infiltration. Regional or distant
667 metastasis, invasive growth or lympho-vascular invasion, tumor size, high mitotic activity, and
668 severe atypia were considered key criteria of malignancy by decreasing order of importance.
669
670 **Whole exome sequencing and copy number alterations**
671 Samples were sequenced to an average depth of 201× and 194× for the tumor and normal
672 samples, respectively. Raw reads were aligned to the mouse reference genome (UCSC mm10)
673 using BWA-MEM. Then, duplicated reads were marked with Picard Tools, and base quality
674 scores were recalibrated using GATK (Van der Auwera *et al*, 2013). Somatic variant calling
675 was performed using 12 different variant callers FreeBayes (Garrison & Marth, 2012), LoFreq,
676 MuSE (Fan *et al*, 2016), Mutect (Cibulskis *et al*, 2013), Mutect2 (McKenna *et al*, 2010), Pindel
677 (Ye *et al*, 2009), Scalpel (Fang *et al*, 2016), Seurat (Christoforides *et al*, 2013), SomaticSniper
678 (Larson *et al*, 2012), Strelka (Kim *et al*, 2018), VarDict (Lai *et al*, 2016), and VarScan2
679 (Koboldt *et al*, 2012). A Panel of Normals (PON) was built using GATK Mutect2. An ensemble
680 approach between the variant callers was used to filter false-positive variants. A minimum of
681 five callers and four callers were required to retain a somatic SNV and indel, respectively.
682 Finally, somatic variants found in the PON were filtered out.

683 Copy number alterations (CNA) were called using VarScan2 Copy Caller. Adjusted log2 ratio
684 were then analyzed with circular binary segmentation as implemented in the DNA copy
685 R/Bioconductor package (Olshen *et al*, 2004) to translate log2ratios measurements in regions
686 of equal copy number. We used a threshold value of 0.1 to call the CNA alterations.
687
688 **Mutagenesis**
689 Single base substitutions (SBSs) were described based on the pyrimidines of the Watson-Crick
690 base pairs, resulting in six major substitution types (C>A, C>G, C>T, T>A, T>C, and T>G).
691 These were further classified across their 16 trinucleotide contexts, defining 96 distinct SBS
692 types.
693
694 **RNA Sequencing and Data Analysis**
695 RNA sequencing was conducted by Novogene (Cambridge, UK). RNA integrity was assessed
696 using the RNA Nano 6000 Assay Kit on a Bioanalyzer 2100 (Agilent Technologies, CA, USA).
697 Total RNA was used for library construction. mRNA was isolated using poly-T oligo-attached
698 magnetic beads and fragmented under elevated temperature in First Strand Synthesis Reaction
699 Buffer. First-strand cDNA was synthesized using random hexamers and M-MuLV Reverse
700 Transcriptase (RNase H-), followed by second-strand synthesis using DNA Polymerase I and
701 RNase H. Overhangs were converted to blunt ends, 3' ends were adenylated, and hairpin-loop
702 adaptors were ligated. Fragments (370–420 bp) were purified using the AMPure XP system
703 (Beckman Coulter), PCR-amplified with Phusion High-Fidelity DNA polymerase, and assessed
704 for quality on the Bioanalyzer 2100. Indexed libraries were clustered using the cBot Cluster
705 Generation System and TruSeq PE Cluster Kit v3-cBot-HS (Illumina), then sequenced on the
706 Illumina NovaSeq platform to generate 150 bp paired-end reads.
707 Sequencing quality was assessed using FastQC
708 ([http://www.bioinformatics.babraham.ac.uk/projects/fastqc/]
709 (http://www.bioinformatics.babraham.ac.uk/projects/fastqc/)) and aggregated across samples
710 with MultiQC (v1.7) (Ewels *et al*, 2016). Reads with a Phred quality score below 30 were
711 filtered out to ensure high data quality.
712 High-quality reads were aligned to a customized mm10 mouse reference genome, including the
713 mCherry transgene, using Subread-align (v1.6.4) (Liao *et al*, 2013) with default parameters.
714 Gene-level counts were quantified with featureCounts (v1.6.4) (Liao *et al*, 2014).
715 Differential expression analysis was performed using DESeq2 (v1.26.0) (Love *et al*, 2014). To
716 account for technical variability, a batch correction was applied based on sequencing run times.
717 Genes with Benjamini–Hochberg adjusted $P < 0.05$ were considered significantly differentially
718 expressed.
719 Principal Component Analysis (PCA) was performed using the prcomp function from R's base
720 `stats` package on variance-stabilized transformed (VST) counts. PCA allowed visualization of
721 sample clustering and assessment of batch effects, ensuring biological replicates grouped
722 together and that batch correction successfully minimized technical variation. GO enrichment
723 analysis was conducted with clusterProfiler (v4.6.0) (Yu *et al*, 2012), focusing on Biological
724 Process (BP) and KEGG pathway categories. A padj ≤ 0.05 was used as the significance
725 threshold, considering an appropriate gene background. Heatmaps were generated using the
726 heatmap.2 function (v3.1.3.1), based on DESeq2-normalized expression values. Venn diagrams

727 were produced using Python's matplotlib venn library. Custom R scripts were used to visualize
728 gene signatures across DESeq2-normalized counts.
729 Ctnnb1 activated and axin1Δ signatures were sourced from Abitbol et al (2018). The Nrf2
730 signature was from (Mitsuishi *et al*, 2012a).
731
732 **Imaging Mass Cytometry**
733 Imaging Mass Cytometry (IMC) was performed using the Hyperion™ Imaging System
734 (Standard BioTools, USA), a multiplexed spatial proteomics platform that enables
735 simultaneous detection of multiple protein markers at subcellular resolution in formalin-fixed
736 paraffin-embedded (FFPE) tissue sections. IMC combines laser ablation with cytometry by
737 time-of-flight (CyTOF) to detect metal-conjugated antibodies, overcoming limitations
738 associated with fluorescence-based imaging such as spectral overlap and tissue
739 autofluorescence (Giesen *et al*, 2014). Mouse liver tumor FFPE sections were processed
740 according to standard protocols including dewaxing, rehydration, and heat-induced antigen
741 retrieval. Sections were stained with a validated panel of 10 metal-tagged antibodies (AMK
742 Biotech) following the steps previously described (Elaldi *et al*, 2021). Nuclear staining was
743 performed using iridium intercalator. Regions of interest (ROIs) of approximately 1 to 2 mm^2
744 were selected on the tissue based on HES-stained sections to ensure representative sampling of
745 both tumor and surrounding liver parenchyma and to avoid necrotic or hemorrhagic areas. Scale
746 bars (200 µm) of the uncropped images are shown in Fig. EV4.
747 Image acquisition was conducted at a spatial resolution of 1 µm using the Hyperion Imaging
748 System. Raw data were exported as OME-TIFF files via the MCD™ Viewer software (Standard
749 BioTools, USA). For each marker of the used IMC-panel noise and background removal was
750 performed using CellProfiler Software to generate an automatic binarization mask used to
751 automatically remove the noise based on a learning-approach of pixel classification. All cleaned
752 images were subsequently reviewed by an expert to ensure the absence of residual noise.
753
754 **Image analysis and quantification**
755 Selected ROIs from denoised images of mice liver tumor sections were analyzed as follows:
756 nuclei were segmented from the DNA1 channel using the legacy Cyto2 model, running on
757 Cellpose 4.0.6 via the napari-serialcellpose plugin (v0.2.2) (Stringer *et al*, 2021). Cellprofiler
758 4.2.8 was used for subsequent quantification of immune marker positivity and relative areas
759 versus total DNA. Metadata were extracted from file names. Integrated intensities of Cellpose-
760 segmented nuclei were calculated for each marker. Since denoising reduced background
761 fluorescence to near zero, any cell exhibiting signal above background was considered positive.
762 The percentage of marker-positive cells relative to total cells (cellpose objects) was calculated
763 per ROI. For area-based measurement, the areas of marker signals above the same threshold
764 were compared relative to total DNA area per ROI. Data means were displayed as bar plots,
765 with the individual ROI means shown as dots. Error bars represent standard error of the mean
766 (s.e.m.). Representative images of segmented ROIs are displayed in figure panels for
767 transparency. Cellprofiler pipelines are available upon request.
768
769 **Ki67 and gH2AX**

Fresh liver was fixed in 10% phosphate-buffered formalin overnight. Paraffin wax sections of 5 µm were prepared for immunostaining (Ki67-abcam ab15580, gH2AX-Merck Millipore 05-636).

Data availability

RNA-seq data are currently being deposited in the Gene Expression Omnibus (GSE).

Acknowledgements

We thank Jean-Charles Graziano from the animal facility, the CRCM Integrative Bioinformatics (Cibi), preclinical TrGET platform, and the Experimental Histology platform (ICEP) for their support and Douglas Maya (IBIS, Sevilla) for helpful discussions. We gratefully acknowledge Frédéric Fiore (CIPHE, Marseille) for his guidance on generating mouse models and Marielle Bréau and Serge Adnot in the initiation of this project. This work has been supported by "La Ligue Nationale Contre le Cancer", Equipe Labellisée, the "Institut National du Cancer" (INCA, PLBIO 2019), the Agence Nationale de la Recherche (ANR) (Grant THALATEL), the cross-cutting Inserm program on aging (AGEMED), the Inserm INTERAGING Program and the National Nature Science Foundation of China (32470830, 92478135).

Author Contributions

L.B. and V.G. coordinated the study in collaboration with C.D. L.B. supervised tumor detection and sampling, prepared mRNA and genomic DNA for WES and RNA-seq analyses with assistance from M.B., and oversaw the generation of paraffin-embedded slides for histology and imaging. J.V. provided all RNA-seq data, while A.G. and F.B. performed WES analyses. P.C. and C.D. conducted the histological characterization of tumors. C.G. and A.M. performed Imaging Mass Cytometry, and T.E. conducted image analysis and quantification in collaboration with C.L. D.C. performed genomic analyses. L.G. performed database analyses, C.D., F.B., C.L and V. G. contributed to study funding. V.G. wrote the manuscript with input from all authors.

Disclosure and competing interest statement

Aïda Meghraoui, CEO of AMK Biotech, and Tom Egger (Quantimagin) have no commercial or financial relationships that could be perceived as a conflict of interest. The remaining authors have declared that no conflict of interest exists.

Figure Legends

Figure 1. Liver tumors collected from p21$^{+/Tert}$ and p21$^{+/TertCi}$ mice.
The histological characteristics of these tumors are summarized in Table 1**.** Tumor sections were stained with anti-Ki67 and anti-gH2AX antibodies. LT4 represents a case of nodular hepatocellular hyperplasia obtained from an aged wild-type (WT) mouse.

Figure 2. Mutational landscape of liver tumors from aged p21$^{+/Tert}$ and p21$^{+/TertCi}$ mice.
a. Somatic mutations in genes found altered in HCC at low or high frequency are idincated. All mutations detected in each tumor are listed in Table S1**.**
b. Copy number alterations in the liver tumors. Chromosomes with gains and loss are indicated in red and green, respectively (see Table S2).
c. Genes recurrently amplified or deleted across tumors.

Figure 3. Mutational signature analysis of p21$^{+/Tert}$ and p21$^{+/TertCi}$ tumors.
a. Number of somatic mutations per exome in the tumors.
b and c. Mutation type in p21$^{+/Tert}$ and p21$^{+/TertCi}$ tumors.
d. Occurrence of mutations from p21$^{+/Tert}$ and p21$^{+/TertCi}$ tumor samples classified by substitution type and trinucleotide context.
e. Heat map showing mutational profiles of individual mouse tumor samples (rows), categorized by substitution type and trinucleotide context (columns).

Figure 4. Transcriptomic analysis of p21$^{+/Tert}$ and p21$^{+/TertCi}$ tumors.
a. Venn diagram showing the number and overlap of significantly ($p<0.05$) upregulated genes (upper panel) or down-regulated (lower panel) between p21$^{+/Tert}$ and p21$^{+/TertCi}$ tumors.
b. Gene Ontology Biological Process (GOBP) terms enriched among differentially expressed genes (DEGs) in p21$^{+/Tert}$ (left) and p21$^{+/TertCi}$ (right) tumors.
c. Expression levels of cyclin dependent kinases and cyclins in p21$^{+/Tert}$ and p21$^{+/TertCi}$ tumors. Statistics *$p<0.05$, **$p<0.01$, *$p<0.001$ vs NT
d-g. Heatmaps showing the expression profiles of pathway-specific gene signatures, including activated β-catenin**,** MAPK–ERK**,** *axin1Δ*, and activated Sonic Hedgehog pathways, in p21$^{+/Tert}$ and p21$^{+/TertCi}$ tumors. Beta-catenin and *axin1*Δ signatures were defined in Abitbol et al (2018).

Figure 5. Downregulation of gluconeogenesis and activation of Nrf2 targets in tumors.
a. Heatmaps showing the expression of genes involved in gluconeogenesis (red group) and glycolysis (Green and Blue groups).
b. Expression levels of FBP1 in p21$^{+/Tert}$ and p21$^{+/TertCi}$ tumors, Statistics *$p<0.05$ vs non tumoral p21$^{+/Tert}$ or p21$^{+/TertCi}$
c. Heatmaps showing the expression of NRF2 target genes. Genes were clustered in two groups: (green) preferentially expressed in beta-catenin activated tumors, (blue) preferentially expressed in MAPK–ERK activated tumors. Arrows indicate genes enhancing antioxidant capacity and glutathione metabolism thereby protecting cells from ferroptosis.

854 **Figure 6. Spatial architecture of liver tumors.**
855 Non tumoral and tumor FFPE tissue sections were analyzed using the Hyperion™ Imaging
856 System with antibodies against CTNNB1 (Yellow), HNF4alpha (Magenta), and α-SMA
857 (Green). L1069 and L982 represent to non-tumoral liver tissue from $p21^{+/Tert}$ and $p21^{+/-}$ mice,
858 respectively. Tumors numbered in the figure are described in Table 1. The number following
859 each tumor name indicates the region of interest (ROI). Iridium intercalator was used for
860 nuclear staining. *High resolution, uncropped images are included in the supplemental files.*
861
862 **Figure 7. Quantification of HNF4alpha and p21 levels across tumor samples.**
863 **a**. ROIs from liver tumor sections were imaged using the Hyperion™ with antibodies against
864 HNF4alpha and p21. Signal quantification was performed as described in the Materials and
865 Methods. The percentage of HNF4alpha, p21, and double-positive cells are shown. The 2 dots
866 for each tumor represent two different ROI.
867 **b.** Representative images of non-tumoral and tumoral sections. HNF4alpha (Green), p21 (Red),
868 and nuclei (Blue).
869 *Mosaic uncropped images are included in the supplemental files.*
870
871 **Figure 8. Tumor infiltration by lymphocyte subsets.**
872 **a.** ROIs were imaged using antibodies against B220, CD3, CD4, CD4 marking B-lymphocytes,
873 T-lymphocytes, auxiliary (helper) T-cells, and cytotoxic T-cells. Signal quantification was
874 performed as described in the Materials and Methods and immune cell infiltration is shown for
875 each tumor.
876 **b**. Representative images of control a: B220 (Green), CD3 (Yellow), CD4 (Magenta), CD8
877 (Cyan) and nuclei (Blue).
878 *Mosaic uncropped images are included in the supplemental files.*
879
880 **Figure 9. Tumor infiltration by macrophages and dendritic cells.**
881 **a.** ROIs were imaged using antibodies against F4/80 and CD11c to label macrophages and
882 dendritic cells, respectively. Signal quantification was performed as described above, and the
883 percentage of positive cells is shown for each tumor.
884 **b.** Representative images of tumor sections. F4/80 is shown in green, CD11c in magenta, and
885 nuclei in blue.
886 *Mosaic uncropped images are included in the supplemental files.*
887
888
889

890 # Table Legends

891

892 ## Table 1. Histological characterization of tumors

Genotype	Mouse	Diagnosis	Main histological features
p21$^{+/Tert}$	662	Liver, Hepatocellular carcinoma.	Moderately differentiated with solid growth pattern.
	663	Liver, Hepatocellular adenoma.	Moderate cytoplasmic vacuolation.
	668	Liver, Hepatocellular carcinoma.	Well differentiated with trabecular to solid growth pattern.
	992	Liver, Hepatocellular adenoma.	
	941	Liver, Hepatocellular carcinoma.	Well differentiated with trabecular to solid growth pattern and multifocal areas of cytoplasmic vacuolation.
	995	Liver, Hepatocellular carcinoma.	Moderately differentiated with solid growth pattern.
	985	Liver, Hemangiosarcoma.	Malignant endothelial tumor with multiple vascular spaces and thrombosis.
	861	Liver, Hematological malignancy.	Diffuse sheets of non-hepatocytic round cells effacing tissue architecture.
	975	Liver, Hematological malignancy.	Diffuse sheets of non-hepatocytic round cells effacing tissue architecture.
	944	Liver, Hematological malignancy.	Diffuse sheets of non-hepatocytic round cells effacing tissue architecture.
	861	Colon, Diffuse large cell lymphoma.	Diffuse sheets of neoplastic lymphoid cells effacing tissue architecture.
p21$^{+/TertCi}$	981	Liver, Hepatocellular carcinoma.	Well differentiated with trabecular to solid growth pattern.
	984	Liver, Hepatocellular adenoma.	Marked diffuse cytoplasmic vacuolation.
	20-1	Liver, Hepatocellular carcinoma.	Well differentiated with trabecular growth pattern.
	20-3	Liver, Hepatocellular carcinoma.	Well differentiated with trabecular growth pattern.
	24	Liver, Hepatocellular carcinoma.	Well differentiated with trabecular to solid growth pattern.
	985	Liver, Hemangiosarcoma.	Malignant endothelial tumor with multiple vascular spaces and thrombosis.
Wild type	WT4	Liver, Non-regenerative nodular hepatocellular hyperplasia.	Nodular proliferation of non-neoplastic hepatocytes that retains lobular architecture and without evidence of liver damage.
	WT5	Liver, Hemangiosarcoma.	Malignant endothelial tumor with multiple vascular spaces and thrombosis.

893
894
895
896
897
898
899
900
901
902
903
904
905
906
907
908
909
910
911
912
913
914
915
916

References

Abitbol S, Dahmani R, Coulouarn C, Ragazzon B, Mlecnik B, Senni N, Savall M, Bossard P, Sohier P, Drouet V, *et al* (2018) AXIN deficiency in human and mouse hepatocytes induces hepatocellular carcinoma in the absence of β-catenin activation. *J Hepatol* 68: 1203–1213

Alexandrov LB, Kim J, Haradhvala NJ, Huang MN, Tian Ng AW, Wu Y, Boot A, Covington KR, Gordenin DA, Bergstrom EN, *et al* (2020) The repertoire of mutational signatures in human cancer. *Nature* 578: 94–101

Bai W, Cheng L, Xiong L, Wang M, Liu H, Yu K & Wang W (2022) Protein succinylation associated with the progress of hepatocellular carcinoma. *J Cell Mol Med* 26: 5702–5712

Bakiri L, Hamacher R, Graña O, Guío-Carrión A, Campos-Olivas R, Martinez L, Dienes HP, Thomsen MK, Hasenfuss SC & Wagner EF (2017) Liver carcinogenesis by FOS-dependent inflammation and cholesterol dysregulation. *J Exp Med* 214: 1387–1409

Bakiri L, Hasenfuss SC, Guío-Carrión A, Thomsen MK, Hasselblatt P & Wagner EF (2024) Liver cancer development driven by the AP-1/c-Jun~Fra-2 dimer through c-Myc. *Proc Natl Acad Sci U S A* 121: e2404188121

Belenguer G, Mastrogiovanni G, Pacini C, Hall Z, Dowbaj AM, Arnes-Benito R, Sljukic A, Prior N, Kakava S, Bradshaw CR, *et al* (2022) RNF43/ZNRF3 loss predisposes to hepatocellular-carcinoma by impairing liver regeneration and altering the liver lipid metabolic ground-state. *Nat Commun* 13: 334

Bhutia YD, Babu E, Ramachandran S & Ganapathy V (2015) Amino Acid transporters in cancer and their relevance to 'glutamine addiction': novel targets for the design of a new class of anticancer drugs. *Cancer Res* 75: 1782–1788

Boiteux S & Radicella JP (2000) The human OGG1 gene: structure, functions, and its implication in the process of carcinogenesis. *Arch Biochem Biophys* 377: 1–8

Braud L, Bernabe M, Vernerey J, Miranda AMA, Dominguez A, Churikov D, Richaud M, Jourquin F, Allan LM, Lachaud C, *et al* (2025) TERT expression attenuates metabolic disorders in obese mice by promoting adipose stem and progenitor cell expansion and differentiation. *Mol Metab*: 102262

Cai J, Zhang P, Cai Y, Zhu G, Chen S, Song L, Du J, Wang B, Dai W, Zhou J, *et al* (2025) Lactylation-Driven NUPR1 Promotes Immunosuppression of Tumor-Infiltrating Macrophages in Hepatocellular Carcinoma. *Adv Sci Weinh Baden-Wurtt Ger* 12: e2413095

Chellappa K, Jankova L, Schnabl JM, Pan S, Brelivet Y, Fung CL-S, Chan C, Dent OF, Clarke SJ, Robertson GR, *et al* (2012) Src tyrosine kinase phosphorylation of nuclear receptor HNF4α correlates with isoform-specific loss of HNF4α in human colon cancer. *Proc Natl Acad Sci U S A* 109: 2302–2307

Chen L, Zhang C, Xue R, Liu M, Bai J, Bao J, Wang Y, Jiang N, Li Z, Wang W, *et al* (2024) Deep whole-genome analysis of 494 hepatocellular carcinomas. *Nature* 627: 586–593

Chen X, Cheng Q, She M, Wang Q, Huang X, Cao L, Fu X & Chen J (2010) Expression of sonic hedgehog signaling components in hepatocellular carcinoma and cyclopamine-induced apoptosis through Bcl-2 downregulation in vitro. *Arch Med Res* 41: 315–323

Chen Y-L, Hung M-H, Chu P-Y, Chao T-I, Tsai M-H, Chen L-J, Hsiao Y-J, Shih C-T, Hsieh F-S & Chen K-F (2017) Protein phosphatase 5 promotes hepatocarcinogenesis through interaction with AMP-activated protein kinase. *Biochem Pharmacol* 138: 49–60

Christoforides A, Carpten JD, Weiss GJ, Demeure MJ, Von Hoff DD & Craig DW (2013) Identification of somatic mutations in cancer through Bayesian-based analysis of sequenced genome pairs. *BMC Genomics* 14: 302

Cibulskis K, Lawrence MS, Carter SL, Sivachenko A, Jaffe D, Sougnez C, Gabriel S, Meyerson M, Lander ES & Getz G (2013) Sensitive detection of somatic point mutations in impure and heterogeneous cancer samples. *Nat Biotechnol* 31: 213–219

Connor F, Rayner TF, Aitken SJ, Feig C, Lukk M, Santoyo-Lopez J & Odom DT (2018) Mutational landscape of a chemically-induced mouse model of liver cancer. *J Hepatol* 69: 840–850

Dantzer C, Vaché J, Brunel A, Mahouche I, Raymond A-A, Dupuy J-W, Petrel M, Bioulac-Sage P, Perrais D, Dugot-Senant N, *et al* (2024) Emerging role of oncogenic ß-catenin in exosome biogenesis as a driver of immune escape in hepatocellular carcinoma. *eLife* 13: RP95191

Delire B & Stärkel P (2015) The Ras/MAPK pathway and hepatocarcinoma: pathogenesis and therapeutic implications. *Eur J Clin Invest* 45: 609–623

Deschl U, Cattley RC, Harada T, Küttler K, Hailey JR, Hartig F, Leblanc B, Marsman DS & Shirai T (2001) Liver, Gallbladder, and Exocrine Pancreas. In *International Classification of Rodent Tumors. The Mouse*, Mohr U (ed) pp 59–86. Berlin, Heidelberg: Springer

Dhanasekaran R, Deutzmann A, Mahauad-Fernandez WD, Hansen AS, Gouw AM & Felsher DW (2022) The MYC oncogene - the grand orchestrator of cancer growth and immune evasion. *Nat Rev Clin Oncol* 19: 23–36

Elaldi R, Hemon P, Petti L, Cosson E, Desrues B, Sudaka A, Poissonnet G, Van Obberghen-Schilling E, Pers J-O, Braud VM, *et al* (2021) High Dimensional Imaging Mass Cytometry Panel to Visualize the Tumor Immune Microenvironment Contexture. *Front Immunol* 12: 666233

Ewels P, Magnusson M, Lundin S & Käller M (2016) MultiQC: summarize analysis results for multiple tools and samples in a single report. *Bioinforma Oxf Engl* 32: 3047–3048

Fan Y, Xi L, Hughes DST, Zhang J, Zhang J, Futreal PA, Wheeler DA & Wang W (2016) MuSE: accounting for tumor heterogeneity using a sample-specific error model improves sensitivity and specificity in mutation calling from sequencing data. *Genome Biol* 17: 178

996 Fan Z, Duan J, Wang L, Xiao S, Li L, Yan X, Yao W, Wu L, Zhang S, Zhang Y, *et al* (2019)
997 PTK2 promotes cancer stem cell traits in hepatocellular carcinoma by activating
998 Wnt/β-catenin signaling. *Cancer Lett* 450: 132–143

999 Fang H, Bergmann EA, Arora K, Vacic V, Zody MC, Iossifov I, O'Rawe JA, Wu Y, Jimenez
1000 Barron LT, Rosenbaum J, *et al* (2016) Indel variant analysis of short-read sequencing
1001 data with Scalpel. *Nat Protoc* 11: 2529–2548

1002 Farazi PA, Glickman J, Horner J & DePinho RA (2006) Cooperative Interactions of p53
1003 Mutation, Telomere Dysfunction, and Chronic Liver Damage in Hepatocellular
1004 Carcinoma Progression. *Cancer Res* 66: 4766–4773

1005 Feng X, Hsu S-J, Bhattacharjee A, Wang Y, Diao J & Price CM (2018) CTC1-STN1
1006 terminates telomerase while STN1-TEN1 enables C-strand synthesis during telomere
1007 replication in colon cancer cells. *Nat Commun* 9: 2827

1008 Fernandez-Banet J, Lee NP, Chan KT, Gao H, Liu X, Sung W-K, Tan W, Fan ST, Poon RT,
1009 Li S, *et al* (2014) Decoding complex patterns of genomic rearrangement in
1010 hepatocellular carcinoma. *Genomics* 103: 189–203

1011 Fujimoto A, Furuta M, Shiraishi Y, Gotoh K, Kawakami Y, Arihiro K, Nakamura T, Ueno M,
1012 Ariizumi S, Hai Nguyen H, *et al* (2015) Whole-genome mutational landscape of liver
1013 cancers displaying biliary phenotype reveals hepatitis impact and molecular diversity.
1014 *Nat Commun* 6: 6120

1015 Garrison E & Marth G (2012) Haplotype-based variant detection from short-read sequencing.
1016 doi:10.48550/arXiv.1207.3907 [PREPRINT]

1017 Ghosh A, Saginc G, Leow SC, Khattar E, Shin EM, Yan TD, Wong M, Zhang Z, Li G, Sung
1018 W-K, *et al* (2012) Telomerase directly regulates NF-κB-dependent transcription. *Nat*
1019 *Cell Biol* 14: 1270–1281

1020 Giannakis M, Hodis E, Jasmine Mu X, Yamauchi M, Rosenbluh J, Cibulskis K, Saksena G,
1021 Lawrence MS, Qian ZR, Nishihara R, *et al* (2014) RNF43 is frequently mutated in
1022 colorectal and endometrial cancers. *Nat Genet* 46: 1264–1266

1023 Giesen C, Wang HAO, Schapiro D, Zivanovic N, Jacobs A, Hattendorf B, Schüffler PJ,
1024 Grolimund D, Buhmann JM, Brandt S, *et al* (2014) Highly multiplexed imaging of
1025 tumor tissues with subcellular resolution by mass cytometry. *Nat Methods* 11: 417–
1026 422

1027 Gu L, Zhu Y, Nandi SP, Lee M, Watari K, Bareng B, Ohira M, Liu Y, Sakane S, Carlessi R,
1028 *et al* (2025) FBP1 controls liver cancer evolution from senescent MASH hepatocytes.
1029 *Nature* 637: 461–469

1030 Gu L, Zhu Y, Watari K, Lee M, Liu J, Perez S, Thai M, Mayfield JE, Zhang B, Cunha E
1031 Rocha K, *et al* (2023) Fructose-1,6-bisphosphatase is a nonenzymatic safety valve that
1032 curtails AKT activation to prevent insulin hyperresponsiveness. *Cell Metab* 35: 1009-
1033 1021.e9

1034 Guo C, You Z, Shi H, Sun Y, Du X, Palacios G, Guy C, Yuan S, Chapman NM, Lim SA, *et*
1035 *al* (2023) SLC38A2 and glutamine signalling in cDC1s dictate anti-tumour immunity.
1036 *Nature* 620: 200–208

1037 Haendeler J, Hoffmann J, Brandes RP, Zeiher AM & Dimmeler S (2003) Hydrogen peroxide
1038 triggers nuclear export of telomerase reverse transcriptase via Src kinase family-
1039 dependent phosphorylation of tyrosine 707. *Mol Cell Biol* 23: 4598–4610

1040 Haendeler Judith, Dröse Stefan, Büchner Nicole, Jakob Sascha, Altschmied Joachim, Goy
1041 Christine, Spyridopoulos Ioakim, Zeiher Andreas M., Brandt Ulrich, & Dimmeler
1042 Stefanie (2009) Mitochondrial Telomerase Reverse Transcriptase Binds to and
1043 Protects Mitochondrial DNA and Function From Damage. *Arterioscler Thromb Vasc*
1044 *Biol* 29: 929–935

1045 Huang C, Santofimia-Castaño P, Liu X, Xia Y, Peng L, Gotorbe C, Neira JL, Tang D,
1046 Pouyssegur J & Iovanna J (2021) NUPR1 inhibitor ZZW-115 induces ferroptosis in a
1047 mitochondria-dependent manner. *Cell Death Discov* 7: 269

1048 Huck I, Gunewardena S, Espanol-Suner R, Willenbring H & Apte U (2019) Hepatocyte
1049 Nuclear Factor 4 Alpha Activation Is Essential for Termination of Liver Regeneration
1050 in Mice. *Hepatol Baltim Md* 70: 666–681

1051 Im J-Y, Kang M-J, Kim B-K & Won M (2023) DDIAS, DNA damage-induced apoptosis
1052 suppressor, is a potential therapeutic target in cancer. *Exp Mol Med* 55: 879–885

1053 Joseph NM, Tsokos CG, Umetsu SE, Shain AH, Kelley RK, Onodera C, Bowman S, Talevich
1054 E, Ferrell LD, Kakar S, *et al* (2019) Genomic profiling of combined hepatocellular-
1055 cholangiocarcinoma reveals similar genetics to hepatocellular carcinoma. *J Pathol*
1056 248: 164–178

1057 Kan Z, Zheng H, Liu X, Li S, Barber TD, Gong Z, Gao H, Hao K, Willard MD, Xu J, *et al*
1058 (2013) Whole-genome sequencing identifies recurrent mutations in hepatocellular
1059 carcinoma. *Genome Res* 23: 1422–1433

1060 Karki A, Putra J, Kim SS, Laquaglia MJ, Perez-Atayde AR, Sadri-Vakili G & Vakili K
1061 (2019) MDM4 expression in fibrolamellar hepatocellular carcinoma. *Oncol Rep* 42:
1062 1487–1496

1063 Kim S, Scheffler K, Halpern AL, Bekritsky MA, Noh E, Källberg M, Chen X, Kim Y, Beyter
1064 D, Krusche P, *et al* (2018) Strelka2: fast and accurate calling of germline and somatic
1065 variants. *Nat Methods* 15: 591–594

1066 Koboldt DC, Zhang Q, Larson DE, Shen D, McLellan MD, Lin L, Miller CA, Mardis ER,
1067 Ding L & Wilson RK (2012) VarScan 2: somatic mutation and copy number alteration
1068 discovery in cancer by exome sequencing. *Genome Res* 22: 568–576

1069 Koh CM, Khattar E, Leow SC, Liu CY, Muller J, Ang WX, Li Y, Franzoso G, Li S, Guccione
1070 E, *et al* (2015) Telomerase regulates MYC-driven oncogenesis independent of its
1071 reverse transcriptase activity. *J Clin Invest* 125: 2109–2122

1072 Koppula P, Zhuang L & Gan B (2021) Cystine transporter SLC7A11/xCT in cancer:
1073 ferroptosis, nutrient dependency, and cancer therapy. *Protein Cell* 12: 599–620

1074 Kotulkar M, Paine-Cabrera D & Apte U (2024) Role of Hepatocyte Nuclear Factor 4 Alpha in
1075 Liver Cancer. *Semin Liver Dis* 44: 383–393

1076 Krauter K, Leinwand L, D'Eustachio P, Ruddle F & Darnell JE (1982) Structural genes of the
1077 mouse major urinary protein are on chromosome 4. *J Cell Biol* 94: 414–417

1078 Lai Z, Markovets A, Ahdesmaki M, Chapman B, Hofmann O, McEwen R, Johnson J,
1079 Dougherty B, Barrett JC & Dry JR (2016) VarDict: a novel and versatile variant caller
1080 for next-generation sequencing in cancer research. *Nucleic Acids Res* 44: e108

1081 Larson DE, Harris CC, Chen K, Koboldt DC, Abbott TE, Dooling DJ, Ley TJ, Mardis ER,
1082 Wilson RK & Ding L (2012) SomaticSniper: identification of somatic point mutations
1083 in whole genome sequencing data. *Bioinforma Oxf Engl* 28: 311–317

1084 Lazarevich NL, Shavochkina DA, Fleishman DI, Kustova IF, Morozova OV, Chuchuev ES &
1085 Patyutko YI (2010) Deregulation of hepatocyte nuclear factor 4 (HNF4)as a marker of
1086 epithelial tumors progression. *Exp Oncol* 32: 167–171

1087 Lee J-E, Wang C, Xu S, Cho Y-W, Wang L, Feng X, Baldridge A, Sartorelli V, Zhuang L,
1088 Peng W, *et al* (2013) H3K4 mono- and di-methyltransferase MLL4 is required for
1089 enhancer activation during cell differentiation. *eLife* 2: e01503

1090 Lee J-S (2015) The mutational landscape of hepatocellular carcinoma. *Clin Mol Hepatol* 21:
1091 220–229

1092 Lehrich BM & Monga SP (2025) WNT-β-catenin signalling in hepatocellular carcinoma:
1093 from bench to clinical trials. *Nat Rev Gastroenterol Hepatol*

1094 Lehrich BM, Tao J, Liu S, Hirsch TZ, Yasaka TM, Cao C, Delgado ER, Guan X, Lu S, Pan L,
1095 *et al* (2024) Development of mutated β-catenin gene signature to identify CTNNB1
1096 mutations from whole and spatial transcriptomic data in patients with HCC. *JHEP Rep*
1097 *Innov Hepatol* 6: 101186

1098 Letouzé E, Shinde J, Renault V, Couchy G, Blanc J-F, Tubacher E, Bayard Q, Bacq D, Meyer
1099 V, Semhoun J, *et al* (2017) Mutational signatures reveal the dynamic interplay of risk
1100 factors and cellular processes during liver tumorigenesis. *Nat Commun* 8: 1315

1101 Li T, Yi J, Wu H, Wang K & Zhou B (2024) SLC7A11 in hepatocellular carcinoma: potential
1102 mechanisms, regulation, and clinical significance. *Am J Cancer Res* 14: 2326–2342

1103 Liao Y, Smyth GK & Shi W (2013) The Subread aligner: fast, accurate and scalable read
1104 mapping by seed-and-vote. *Nucleic Acids Res* 41: e108

1105 Liao Y, Smyth GK & Shi W (2014) featureCounts: an efficient general purpose program for
1106 assigning sequence reads to genomic features. *Bioinforma Oxf Engl* 30: 923–930

1107 Lipskaia L, Breau M, Cayrou C, Churikov D, Braud L, Jacquet J, Born E, Fouillade C,
1108 Curras-Alonso S, Bauwens S, *et al* (2024) mTert induction in p21-positive cells
1109 counteracts capillary rarefaction and pulmonary emphysema. *EMBO Rep*: 1–35

1110 Love MI, Huber W & Anders S (2014) Moderated estimation of fold change and dispersion
1111 for RNA-seq data with DESeq2. *Genome Biol* 15: 550

1112 Luchkova A, Mata A & Cadenas S (2024) Nrf2 as a regulator of energy metabolism and
1113 mitochondrial function. *FEBS Lett* 598: 2092–2105

1114 Luo W, Peterson A, Garcia BA, Coombs G, Kofahl B, Heinrich R, Shabanowitz J, Hunt DF,
1115 Yost HJ & Virshup DM (2007) Protein phosphatase 1 regulates assembly and function
1116 of the beta-catenin degradation complex. *EMBO J* 26: 1511–1521

1117 Malhotra D, Portales-Casamar E, Singh A, Srivastava S, Arenillas D, Happel C, Shyr C,
1118 Wakabayashi N, Kensler TW, Wasserman WW, *et al* (2010) Global mapping of
1119 binding sites for Nrf2 identifies novel targets in cell survival response through ChIP-
1120 Seq profiling and network analysis. *Nucleic Acids Res* 38: 5718–5734

1121 Mallette FA, Mattiroli F, Cui G, Young LC, Hendzel MJ, Mer G, Sixma TK & Richard S
1122 (2012) RNF8- and RNF168-dependent degradation of KDM4A/JMJD2A triggers
1123 53BP1 recruitment to DNA damage sites. *EMBO J* 31: 1865–1878

1124 McKenna A, Hanna M, Banks E, Sivachenko A, Cibulskis K, Kernytsky A, Garimella K,
1125 Altshuler D, Gabriel S, Daly M, *et al* (2010) The Genome Analysis Toolkit: a
1126 MapReduce framework for analyzing next-generation DNA sequencing data. *Genome*
1127 *Res* 20: 1297–1303

1128 Mishima M, Takai A, Takeda H, Iguchi E, Nakano S, Fujii Y, Ueno M, Ito T, Teramura M,
1129 Eso Y, *et al* (2024) TERT upregulation promotes cell proliferation via degradation of
1130 p21 and increases carcinogenic potential. *J Pathol* 264: 318–331

1131 Mitsuishi Y, Motohashi H & Yamamoto M (2012a) The Keap1-Nrf2 system in cancers: stress
1132 response and anabolic metabolism. *Front Oncol* 2: 200

1133 Mitsuishi Y, Taguchi K, Kawatani Y, Shibata T, Nukiwa T, Aburatani H, Yamamoto M &
1134 Motohashi H (2012b) Nrf2 redirects glucose and glutamine into anabolic pathways in
1135 metabolic reprogramming. *Cancer Cell* 22: 66–79

1136 Montironi C, Castet F, Haber PK, Pinyol R, Torres-Martin M, Torrens L, Mesropian A, Wang
1137 H, Puigvehi M, Maeda M, *et al* (2023) Inflamed and non-inflamed classes of HCC: a
1138 revised immunogenomic classification. *Gut* 72: 129–140

1139 Nault JC, Calderaro J, Di Tommaso L, Balabaud C, Zafrani ES, Bioulac-Sage P, Roncalli M
1140 & Zucman-Rossi J (2014) Telomerase reverse transcriptase promoter mutation is an
1141 early somatic genetic alteration in the transformation of premalignant nodules in
1142 hepatocellular carcinoma on cirrhosis. *Hepatology* 60: 1983

1143 Nault JC, Mallet M, Pilati C, Calderaro J, Bioulac-Sage P, Laurent C, Laurent A, Cherqui D,
1144 Balabaud C, Zucman-Rossi J, *et al* (2013) High frequency of telomerase reverse-
1145 transcriptase promoter somatic mutations in hepatocellular carcinoma and
1146 preneoplastic lesions. *Nat Commun* 4: 2218

1147 Nault J-C, Ningarhari M, Rebouissou S & Zucman-Rossi J (2019) The role of telomeres and
1148 telomerase in cirrhosis and liver cancer. *Nat Rev Gastroenterol Hepatol* 16: 544–558

1149 Ni F-B, Lin Z, Fan X-H, Shi K-Q, Ao J-Y, Wang X-D & Chen R-C (2020) A novel genomic-
1150 clinicopathologic nomogram to improve prognosis prediction of hepatocellular
1151 carcinoma. *Clin Chim Acta Int J Clin Chem* 504: 88–97

1152 Niu Z-S, Niu X-J & Wang W-H (2016) Genetic alterations in hepatocellular carcinoma: An
1153 update. *World J Gastroenterol* 22: 9069–9095

1154 Olshen AB, Venkatraman ES, Lucito R & Wigler M (2004) Circular binary segmentation for
1155 the analysis of array-based DNA copy number data. *Biostat Oxf Engl* 5: 557–572

1156 Pang J-S, Bai X-M, Wan W-J, Kang T, Wen R, Li L-P, Yin H-H, Lu C-M, Wen D-Y, He Y,
1157 *et al* (2024) RAD21: A Key Transcriptional Regulator in the Development of Residual
1158 Liver Cancer. *J Hepatocell Carcinoma* 11: 285–304

1159 Park J-I, Venteicher AS, Hong JY, Choi J, Jun S, Shkreli M, Chang W, Meng Z, Cheung P, Ji
1160 H, *et al* (2009) Telomerase modulates Wnt signalling by association with target gene
1161 chromatin. *Nature* 460: 66–72

1162 Paturel A, Hall J & Chemin I (2022) Poly(ADP-Ribose) Polymerase Inhibition as a Promising
1163 Approach for Hepatocellular Carcinoma Therapy. *Cancers* 14: 3806

1164 Ramos-Santillan V, Oshi M, Nelson E, Endo I & Takabe K (2024) High Ki67 Gene
1165 Expression Is Associated With Aggressive Phenotype in Hepatocellular Carcinoma.
1166 *World J Oncol* 15: 257–267

1167 Rebouissou S, Franconi A, Calderaro J, Letouzé E, Imbeaud S, Pilati C, Nault J-C, Couchy G,
1168 Laurent A, Balabaud C, *et al* (2016) Genotype-phenotype correlation of CTNNB1
1169 mutations reveals different ß-catenin activity associated with liver tumor progression.
1170 *Hepatol Baltim Md* 64: 2047–2061

1171 Reimann M, Lee S & Schmitt CA (2024) Cellular senescence: Neither irreversible nor
1172 reversible. *J Exp Med* 221: e20232136

1173 Ruiz de Galarreta M, Bresnahan E, Molina-Sánchez P, Lindblad KE, Maier B, Sia D,
1174 Puigvehi M, Miguela V, Casanova-Acebes M, Dhainaut M, *et al* (2019) β-Catenin
1175 Activation Promotes Immune Escape and Resistance to Anti-PD-1 Therapy in
1176 Hepatocellular Carcinoma. *Cancer Discov* 9: 1124–1141

1177 Sanz-Moreno A, Becker L, Xie K, da Silva-Buttkus P, Dragano NRV, Aguilar-Pimentel A,
1178 Amarie OV, Calzada-Wack J, Kraiger M, Leuchtenberger S, *et al* (2025) Loss of Ten1
1179 in mice induces telomere shortening and models human dyskeratosis congenita. *Sci*
1180 *Adv* 11: eadp8093

1181 Saretzki G (2014) Extra-telomeric functions of human telomerase: cancer, mitochondria and
1182 oxidative stress. *Curr Pharm Des* 20: 6386–6403

1183 Schaeffer S, Gupta B, Calatayud A-L, Calderaro J, Caruso S, Hirsch TZ, Pelletier L, Zucman-
1184 Rossi J & Rebouissou S (2023) RSK2 inactivation cooperates with AXIN1
1185 inactivation or β-catenin activation to promote hepatocarcinogenesis. *J Hepatol* 79:
1186 704–716

1187 Schulze K, Imbeaud S, Letouzé E, Alexandrov LB, Calderaro J, Rebouissou S, Couchy G,
1188 Meiller C, Shinde J, Soysouvanh F, *et al* (2015) Exome sequencing of hepatocellular
1189 carcinomas identifies new mutational signatures and potential therapeutic targets. *Nat*
1190 *Genet* 47: 505–511

1191 Schulze K, Nault J-C & Villanueva A (2016) Genetic profiling of hepatocellular carcinoma
1192 using next-generation sequencing. *J Hepatol* 65: 1031–1042

1193 Ségal-Bendirdjian E & Geli V (2019) Non-canonical Roles of Telomerase: Unraveling the
1194 Imbroglio. *Front Cell Dev Biol* 7

1195 Shokouhian B, Negahdari B, Heydari Z, Totonchi M, Aboulkheyr Es H, Piryaei A, Mostafavi
1196 E & Vosough M (2023) HNF4α is possibly the missing link between epithelial-
1197 mesenchymal transition and Warburg effect during hepatocarcinogenesis. *Cancer Sci*
1198 114: 1337–1352

1199 Snow BE, Mateyak M, Paderova J, Wakeham A, Iorio C, Zakian V, Squire J & Harrington L
1200 (2007) Murine Pif1 interacts with telomerase and is dispensable for telomere function
1201 in vivo. *Mol Cell Biol* 27: 1017–1026

1202 Stringer C, Wang T, Michaelos M & Pachitariu M (2021) Cellpose: a generalist algorithm for
1203 cellular segmentation. *Nat Methods* 18: 100–106

1204 Su Z, Liu Y, Wang L & Gu W (2025) Regulation of SLC7A11 as an unconventional
1205 checkpoint in tumorigenesis through ferroptosis. *Genes Dis* 12: 101254

1206 Sun B, Lei X, Cao M, Li Y & Yang L-Y (2023) Hepatocellular carcinoma cells remodel the
1207 pro-metastatic tumour microenvironment through recruitment and activation of
1208 fibroblasts via paracrine Egfl7 signaling. *Cell Commun Signal CCS* 21: 180

1209 Sun X, Liu Y, Cheng C, Sun H & Tian L (2024) CTHRC1 modulates cell proliferation and
1210 invasion in hepatocellular carcinoma by DNA methylation. *Discov Oncol* 15: 347

1211 Sung W-K, Zheng H, Li S, Chen R, Liu X, Li Y, Lee NP, Lee WH, Ariyaratne PN,
1212 Tennakoon C, *et al* (2012) Genome-wide survey of recurrent HBV integration in
1213 hepatocellular carcinoma. *Nat Genet* 44: 765–769

1214 Tambay V, Raymond V-A, Voisin L, Meloche S & Bilodeau M (2024) Reprogramming of
1215 Glutamine Amino Acid Transporters Expression and Prognostic Significance in
1216 Hepatocellular Carcinoma. *Int J Mol Sci* 25: 7558

1217 Tang B, Wang Y, Zhu J, Song J, Fang S, Weng Q, Yang Y, Tu J, Zhao Z, Chen M, *et al*
1218 (2023) TACE responser NDRG1 acts as a guardian against ferroptosis to drive
1219 tumorgenesis and metastasis in HCC. *Biol Proced Online* 25: 13

1220 Tate JG, Bamford S, Jubb HC, Sondka Z, Beare DM, Bindal N, Boutselakis H, Cole CG,
1221 Creatore C, Dawson E, *et al* (2019) COSMIC: the Catalogue Of Somatic Mutations In
1222 Cancer. *Nucleic Acids Res* 47: D941–D947

1223 Thoolen B, Maronpot RR, Harada T, Nyska A, Rousseaux C, Nolte T, Malarkey DE,
1224 Kaufmann W, Küttler K, Deschl U, *et al* (2010) Proliferative and nonproliferative
1225 lesions of the rat and mouse hepatobiliary system. *Toxicol Pathol* 38: 5S-81S

1226 Totoki Y, Tatsuno K, Covington KR, Ueda H, Creighton CJ, Kato M, Tsuji S, Donehower
1227 LA, Slagle BL, Nakamura H, *et al* (2014) Trans-ancestry mutational landscape of
1228 hepatocellular carcinoma genomes. *Nat Genet* 46: 1267–1273

1229 Van der Auwera GA, Carneiro MO, Hartl C, Poplin R, Del Angel G, Levy-Moonshine A,
1230 Jordan T, Shakir K, Roazen D, Thibault J, *et al* (2013) From FastQ data to high
1231 confidence variant calls: the Genome Analysis Toolkit best practices pipeline. *Curr*
1232 *Protoc Bioinforma* 43: 11.10.1-11.10.33

1233 Villanueva A, Alsinet C, Yanger K, Hoshida Y, Zong Y, Toffanin S, Rodriguez-Carunchio L,
1234 Solé M, Thung S, Stanger BZ, *et al* (2012) Notch signaling is activated in human
1235 hepatocellular carcinoma and induces tumor formation in mice. *Gastroenterology* 143:
1236 1660-1669.e7

1237 Wang F, Stewart JA, Kasbek C, Zhao Y, Wright WE & Price CM (2012) Human CST has
1238 independent functions during telomere duplex replication and C-strand fill-in. *Cell*
1239 *Rep* 2: 1096–1103

1240 Wang K, Yuen ST, Xu J, Lee SP, Yan HHN, Shi ST, Siu HC, Deng S, Chu KM, Law S, *et al*
1241 (2014) Whole-genome sequencing and comprehensive molecular profiling identify
1242 new driver mutations in gastric cancer. *Nat Genet* 46: 573–582

1243 Wang Y, Zeng J, Chen W, Fan J, Hylemon PB & Zhou H (2023) Long Noncoding RNA H19:
1244 A Novel Oncogene in Liver Cancer. *Non-Coding RNA* 9: 19

1245 Wu H, Reizel T, Wang YJ, Lapiro JL, Kren BT, Schug J, Rao S, Morgan A, Herman A,
1246 Shekels LL, *et al* (2020) A negative reciprocal regulatory axis between cyclin D1 and
1247 HNF4α modulates cell cycle progression and metabolism in the liver. *Proc Natl Acad*
1248 *Sci U S A* 117: 17177–17186

1249 Xiao H, Tong R, Ding C, Lv Z, Du C, Peng C, Cheng S, Xie H, Zhou L, Wu J, *et al* (2014) γ-
1250 H2AX promotes hepatocellular carcinoma angiogenesis via EGFR/HIF-1α/VEGF
1251 pathways under hypoxic condition. *Oncotarget* 6: 2180–2192

1252 Xu H, Zhao J, Li J, Zhu Z, Cui Z, Liu R, Lu R, Yao Z & Xu Q (2022) Cancer associated
1253 fibroblast-derived CCL5 promotes hepatocellular carcinoma metastasis through
1254 activating HIF1α/ZEB1 axis. *Cell Death Dis* 13: 478

1255 Xu Y, Ji Y, Li X, Ding J, Chen L, Huang Y & Wei W (2021) URI1 suppresses irradiation-
1256 induced reactive oxygen species (ROS) by activating autophagy in hepatocellular
1257 carcinoma cells. *Int J Biol Sci* 17: 3091–3103

1258 Yang Z, Liu J, Xue F, Zhang L, Xue H, Wu Y, Bai S, Du F, Wang X, Deng W, *et al* (2023)
1259 Genomic landscape of Chinese patients with hepatocellular carcinoma using next-
1260 generation sequencing and its association with the prognosis. *Ann Hepatol* 28: 100898

1261 Ye K, Schulz MH, Long Q, Apweiler R & Ning Z (2009) Pindel: a pattern growth approach
1262 to detect break points of large deletions and medium sized insertions from paired-end
1263 short reads. *Bioinforma Oxf Engl* 25: 2865–2871

1264 Yu G, Wang L-G, Han Y & He Q-Y (2012) clusterProfiler: an R package for comparing
1265 biological themes among gene clusters. *Omics J Integr Biol* 16: 284–287

1266 Zhang G, Xiao Y, Liu H, Wu Y, Xue M & Li J (2024a) Integrated machine learning screened
1267 glutamine metabolism-associated biomarker SLC1A5 to predict immunotherapy
1268 response in hepatocellular carcinoma. *Immunobiology* 229: 152841

1269 Zhang G, Xiao Y, Tan J, Liu H, Fan W & Li J (2024b) Elevated SLC1A5 associated with
1270 poor prognosis and therapeutic resistance to transarterial chemoembolization in
1271 hepatocellular carcinoma. *J Transl Med* 22: 543

1272 Zhang J, Rane G, Dai X, Shanmugam MK, Arfuso F, Samy RP, Lai MKP, Kappei D, Kumar
1273 AP & Sethi G (2016) Ageing and the telomere connection: An intimate relationship
1274 with inflammation. *Ageing Res Rev* 25: 55–69

1275 Zhang Y, Jiang H-H, Wang Z-Y, Zhai B & Lin M-B (2023) Alcohol dehydrogenase 4 is a
1276 TP53-associated gene signature for the prediction of prognosis in hepatocellular
1277 carcinoma. *Oncol Lett* 25: 3

1278 Zhang Y, Qiu Z, Wei L, Tang R, Lian B, Zhao Y, He X & Xie L (2014) Integrated analysis of
1279 mutation data from various sources identifies key genes and signaling pathways in
1280 hepatocellular carcinoma. *PloS One* 9: e100854

1281 Zhang Y, Wang D, Chen X, Wang Y, Zhang G & Liu X (2025) A pan-cancer perspective
1282 analysis reveals the prognostic significance of SLC7A11 in hepatocellular carcinoma.
1283 *Front Oncol* 15: 1601140

1284 Zhong FL, Batista LFZ, Freund A, Pech MF, Venteicher AS & Artandi SE (2012) TPP1 OB-
1285 fold domain controls telomere maintenance by recruiting telomerase to chromosome
1286 ends. *Cell* 150: 481–494

1287 Zhu Y, Wei D, Karin M & Gu L (2025) The FBP1-TP53-NRF2 metabolic switch in
1288 metabolic dysfunction-associated steatohepatitis-hepatocellular carcinoma progression
1289 and senescence reversal. *Clin Transl Med* 15: e70293

1290 Zucman-Rossi J, Villanueva A, Nault J-C & Llovet JM (2015) Genetic Landscape and
1291 Biomarkers of Hepatocellular Carcinoma. *Gastroenterology* 149: 1226-1239.e4

1292
1293
1294

	Tumor	Type	H&E	Ki67		gH2AX	
p21^{Tert}	LT662	HCC			++		++
	LT663	HCC			++		++
	LT668	HCC			++		+
	LT941	HCC			+++		+++
	LT992	HCA			+		+
p21^{TertCi}	LT981	HCC			++		++
	LT984	HCA			+		+
	LT24	HCC			++		++
	LT20-1	HCC			++		++
	LT20-3	HCC			+		+
WT	LT4	Liver HP			+		+

Figure 1

A

	Tumor	Somatic mutations			
p21^{Tert}	LT662	Ctnnb1 Asp32Tyr	Kdm4d Gln73His	Col11a1 Glu1155Lys	
	LT663	Ctnnb1 Thr41Ile	Kdm3c Arg278Gly	Ddias Pro706Leu	
	LT941	Egfr Ser303Tyr	Ptpn5 Arg246Gly	Ppp1r1a Splicing var	
	LT992		Ppp1r9a Leu1273fs	Ptpre Gln639del	Sucla2 Gln87del
p21^{TertCi}	LT981	Hras Gln61Lys	Rnf43 Thr208Pro		
	LT984	Ep300 Ala74Glu	Rnf168 Glu159Del	Fn1 Cys335Gly	
	LT24	Hras Gln61Lys	Ogg1 Cys253Ter		
	LT20-1	Ep300 Ala74Glu	Ppp1ca Arg191Trp	Uri1^{Ser481fs}	
	LT20-3	Hras Gln61Lys Ep300 Ala74Glu	Kmt2d Gln4282de	Fga Ala245fs	
WT	LT4	Ctnnb1^{Ser} 45Phe	Rnf19a Lys58fs		

B

	Tumor	Gain/Loss
p21^{Tert}	LT662	Chr **15**, 18 Chr**4**, 13, 11, 19
	LT663	Chr 6, **15**, **X**, Chr 14 chromothripsis
	LT941	Chr 1**, 5**, **X** Chr3, 8, 9, 13
	LT992	No CNA
p21^{TertCi}	LT981	Chr 1**, 5**, 10, **15**, 16, 17, 18, Chr **4**, 8, 1, 14, 19, X
	LT984	No CNA
	LT24	Chr 7,**15**, 19 Chr3, **4**, 6, 9, 10, 11, 12, 13, 14, 17, 18, X
	LT20-1	dispersed CNA
	LT20-3	dispersed CNA
WT	LT4	Chr **4**, 18, X

C

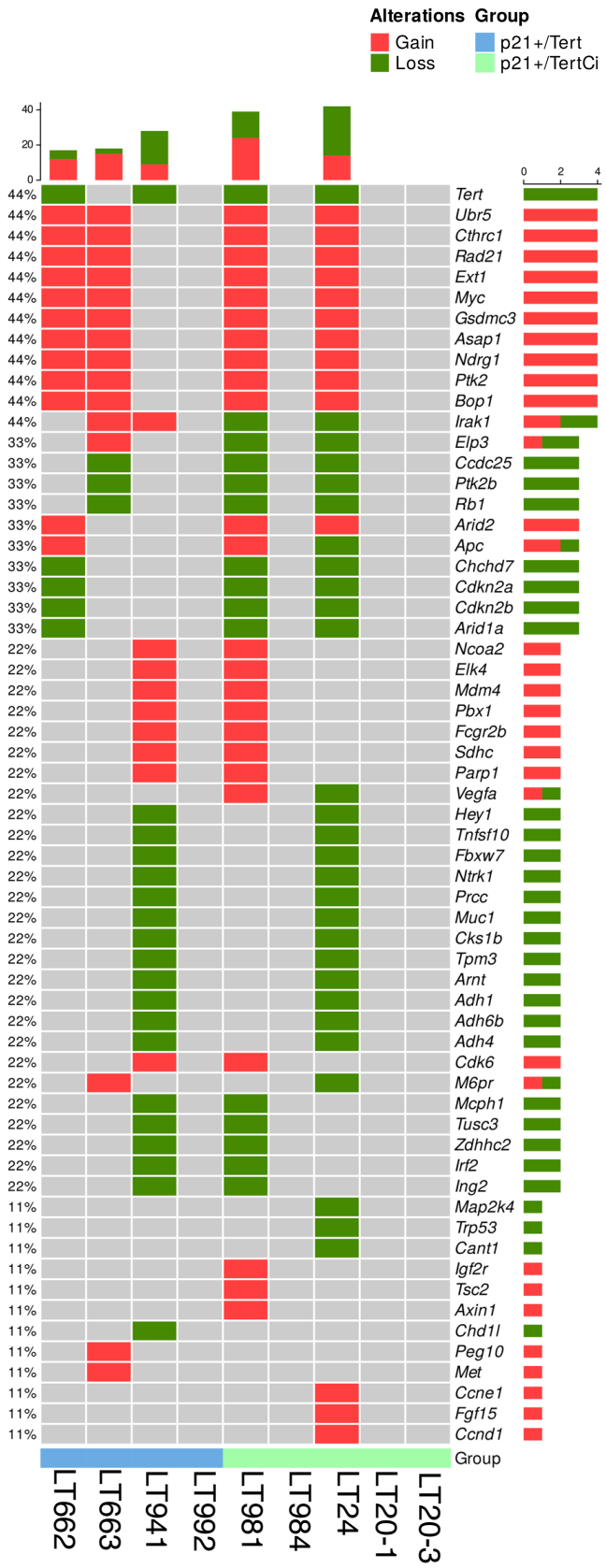

Figure 2

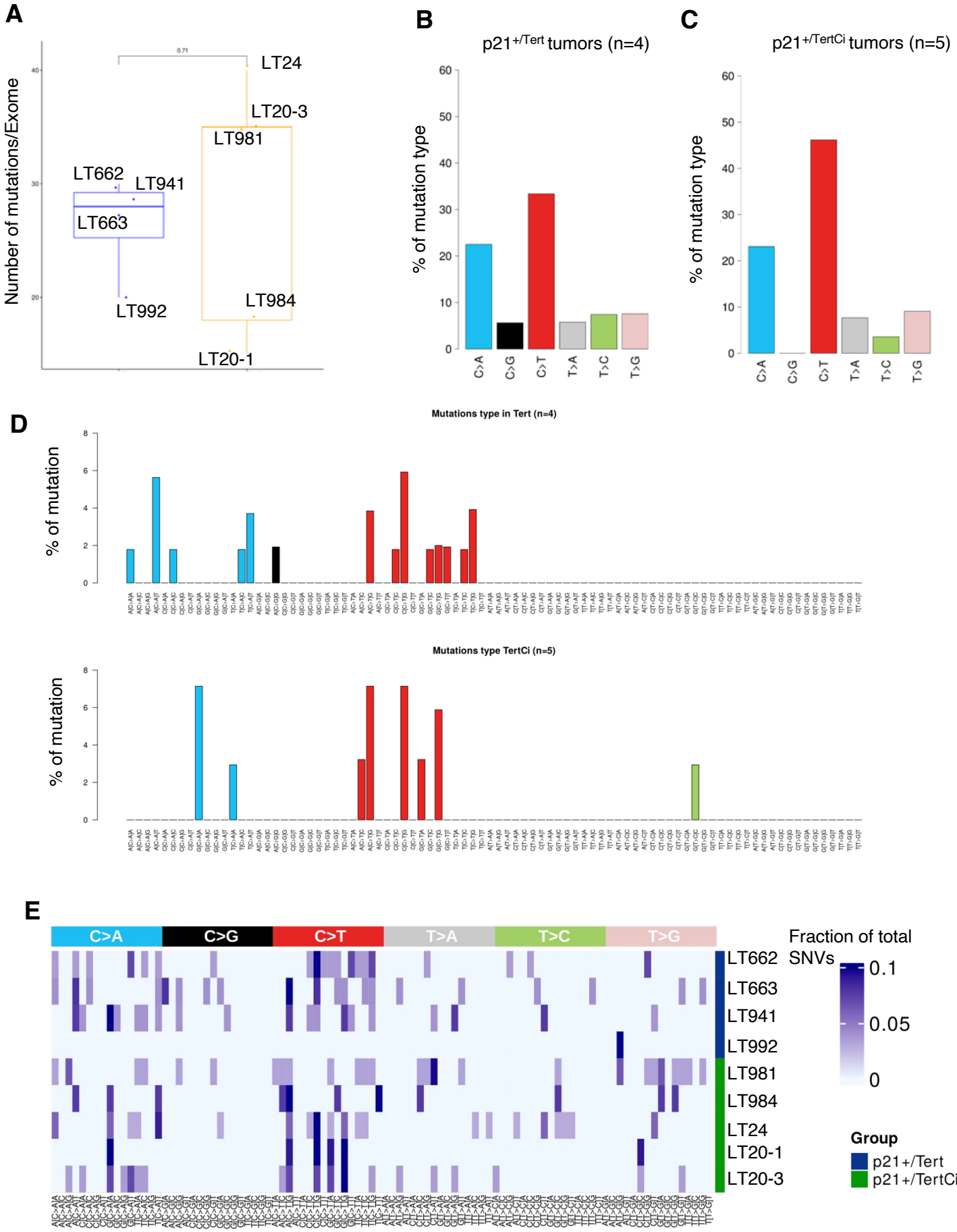
A
Number of mutations/Exome
0.71
LT24
LT20-3
LT981
LT662
LT941
LT663
LT992
LT984
LT20-1
B
p21+/Tert tumors (n=4)
% of mutation type
C>A
C>G
C>T
T>A
T>C
T>G
C
p21+/TertCi tumors (n=5)
% of mutation type
D
Mutations type in Tert (n=4)
% of mutation
Mutations type TertCi (n=5)
% of mutation
E
C>A
C>G
C>T
T>A
T>C
T>G
LT662
LT663
LT941
LT992
LT981
LT984
LT24
LT20-1
LT20-3
Fraction of total SNVs
0.1
0.05
0
Group
p21+/Tert
p21+/TertCi

Figure 3

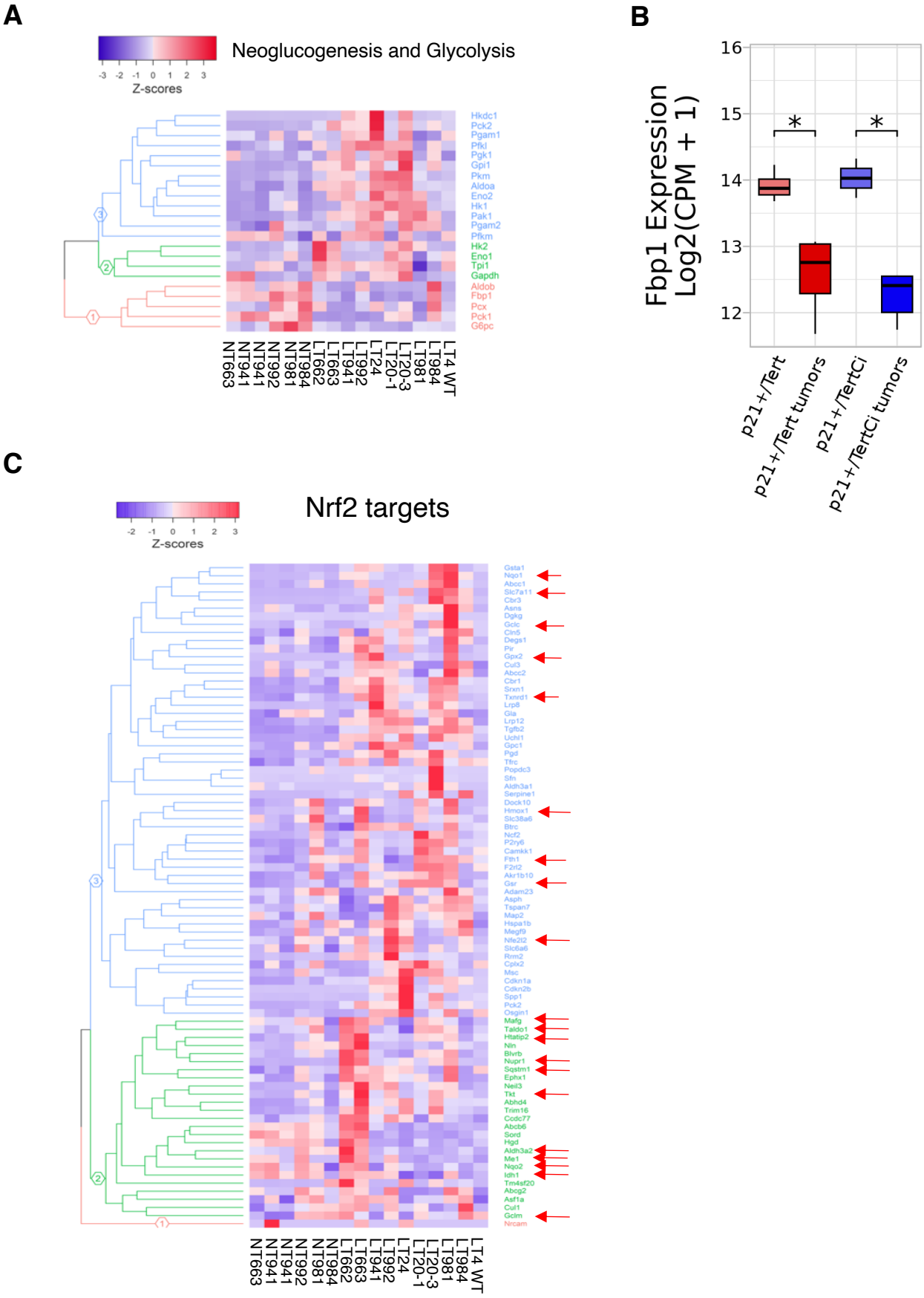
A
Neoglucogenesis and Glycolysis
-3 -2 -1 0 1 2 3
Z-scores
Hkdc1
Pck2
Pgam1
Pfkl
Pgk1
Gpi1
Pkm
Aldoa
Eno2
Hk1
Pak1
Pgam2
Pfkm
Hk2
Eno1
Tpi1
Gapdh
Aldob
Fbp1
Pcx
Pck1
G6pc
NT663
NT941
NT941
NT992
NT981
NT984
LT662
LT663
LT941
LT992
LT24
LT20-1
LT20-3
LT981
LT984
LT4 WT
B
Fbp1 Expression
Log2(CPM + 1)
16
15
14
13
12
*
*
p21+/Tert
p21+/Tert tumors
p21+/TertCi
p21+/TertCi tumors
C
Nrf2 targets
-2 -1 0 1 2 3
Z-scores
Gsta1
Nqo1
Abcc1
Slc7a11
Cbr3
Asns
Dgkg
Gclc
Ciri5
Degs1
Pir
Gpx2
Cul3
Abcc2
Cbr1
Srxn1
Txnrd1
Lrp8
Gla
Lrp12
Tgfb2
Uchl1
Gpc1
Pgd
Tfrc
Popdc3
Sfn
Aldh3a1
Serpine1
Dock10
Hmox1
Slc38a6
Btrc
Ncf2
P2ry6
Camkk1
Fth1
F2rl2
Akr1b10
Gsr
Adam23
Asph
Tspan7
Map2
Hspa1b
Megf9
Nfe2l2
Slc6a6
Rrm2
Cpkx2
Msc
Cdkn1a
Cdkn2b
Spp1
Pck2
Osgin1
Mafg
Taldo1
Hsfip2
Nln
Blvrb
Nupr1
Sqstm1
Ephx1
Neil3
Tkt
Abhd4
Trim16
Ccdc77
Abcb6
Sord
Hgd
Aldh3a2
Me1
Nqo2
Idh1
Tm4sf20
Abcg2
Asf1a
Cul1
Gclm
Nrcam
NT663
NT941
NT941
NT992
NT981
NT984
LT662
LT663
LT941
LT992
LT24
LT20-1
LT20-3
LT981
LT984
LT4 WT

Figure 5.

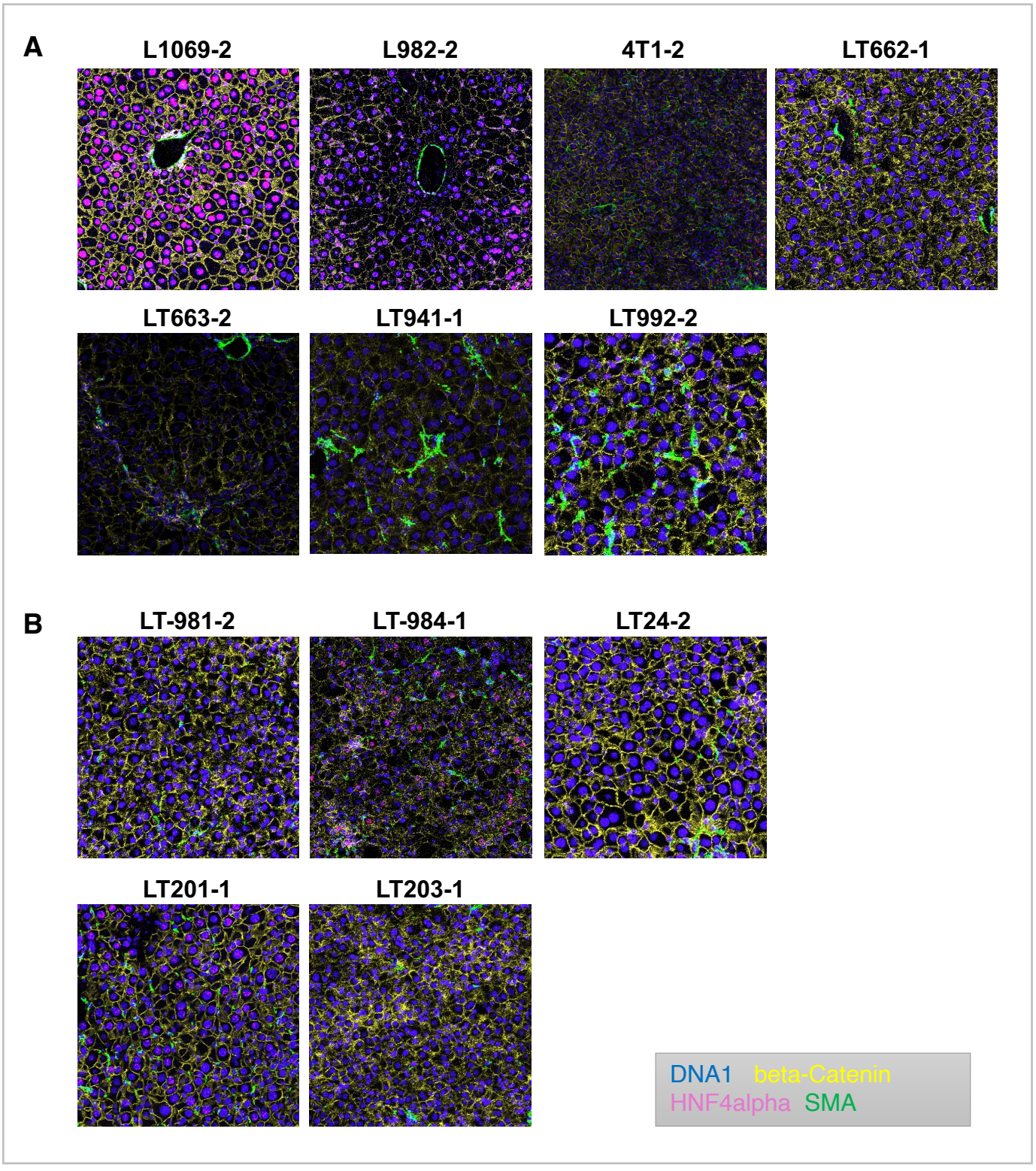
A
L1069-2
L982-2
4T1-2
LT662-1
LT663-2
LT941-1
LT992-2
B
LT-981-2
LT-984-1
LT24-2
LT201-1
LT203-1
DNA1
beta-Catenin
HNF4alpha
SMA

Figure 6.

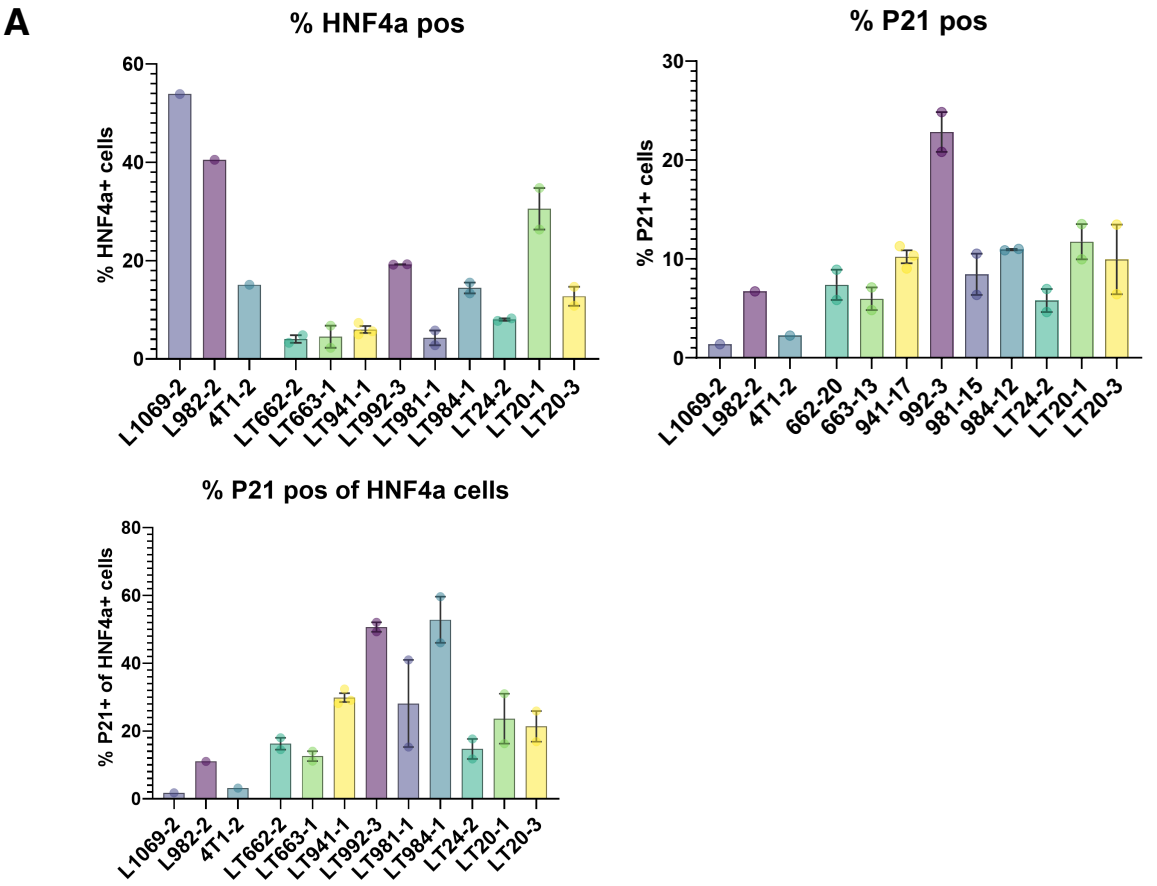
A
% HNF4a pos
% HNF4a+ cells
60
40
20
0
L1069-2
L982-2
4T1-2
LT662-2
LT663-1
LT941-1
LT992-3
LT981-1
LT984-1
LT24-2
LT20-1
LT20-3
% P21 pos
% P21+ cells
30
20
10
0
L1069-2
L982-2
4T1-2
662-20
663-13
941-17
992-3
981-15
984-12
LT24-2
LT20-1
LT20-3
% P21 pos of HNF4a cells
% P21+ of HNF4a+ cells
80
60
40
20
0
L1069-2
L982-2
4T1-2
LT662-2
LT663-1
LT941-1
LT992-3
LT981-1
LT984-1
LT24-2
LT20-1
LT20-3

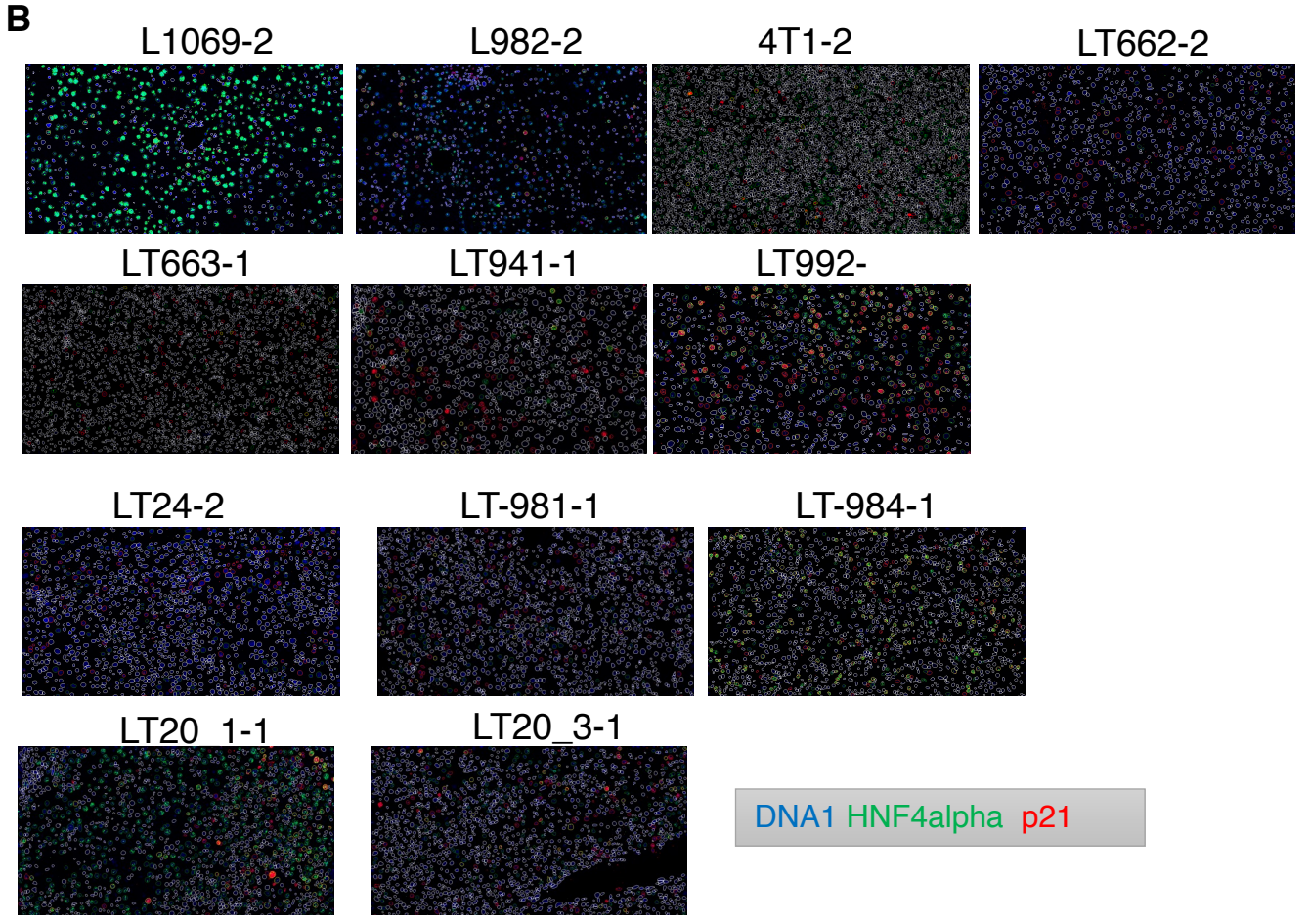
B
L1069-2
L982-2
4T1-2
LT662-2
LT663-1
LT941-1
LT992-
LT24-2
LT-981-1
LT-984-1
LT20_1-1
LT20_3-1
DNA1 HNF4alpha p21

Figure 7.

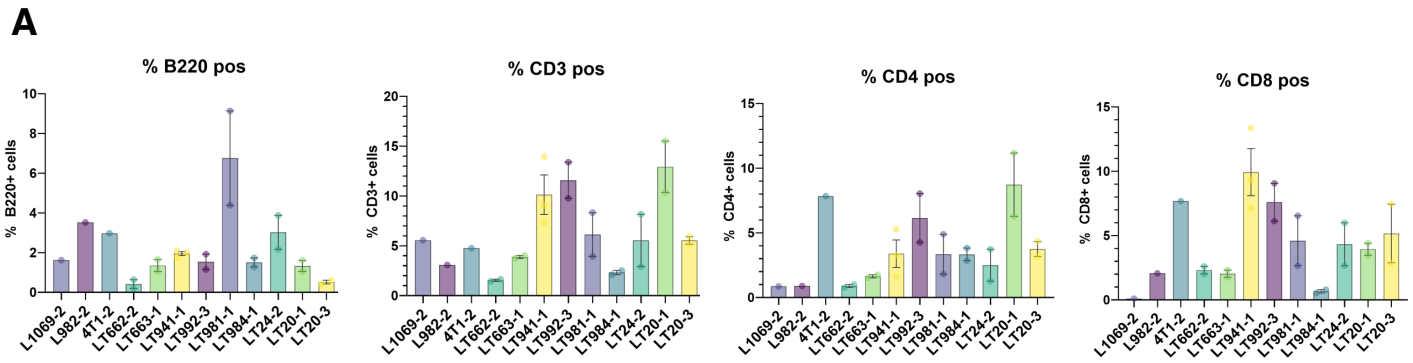
A
% B220 pos
% B220+ cells
% CD3 pos
% CD3+ cells
% CD4 pos
% CD4+ cells
% CD8 pos
% CD8+ cells
L1069-2
L982-2
4T1-2
LT662-2
LT663-1
LT941-1
LT992-3
LT981-1
LT984-1
LT24-2
LT20-1
LT20-3

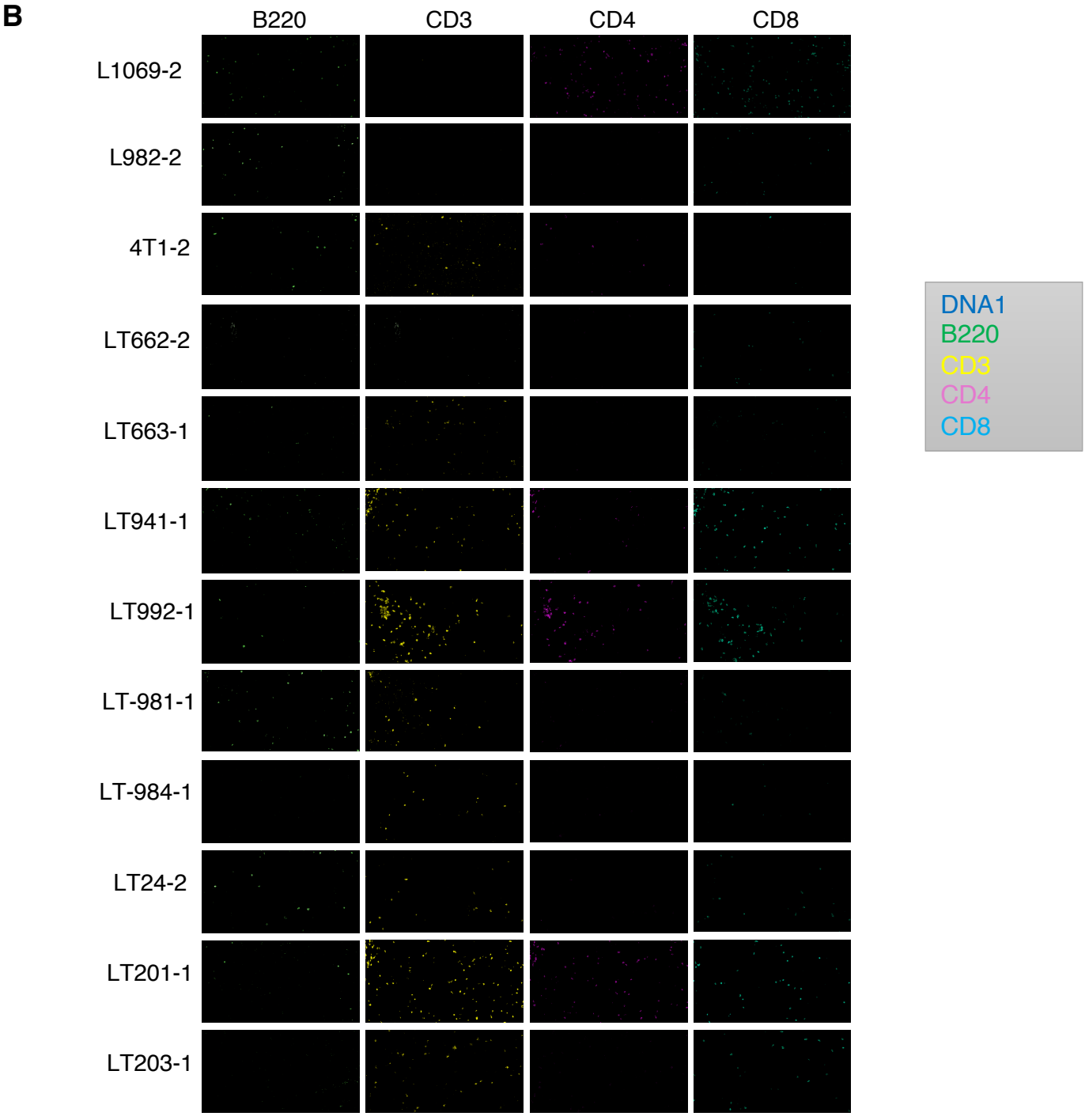
B
B220
CD3
CD4
CD8
L1069-2
L982-2
4T1-2
LT662-2
LT663-1
LT941-1
LT992-1
LT-981-1
LT-984-1
LT24-2
LT201-1
LT203-1
DNA1
B220
CD3
CD4
CD8

Figure 8.

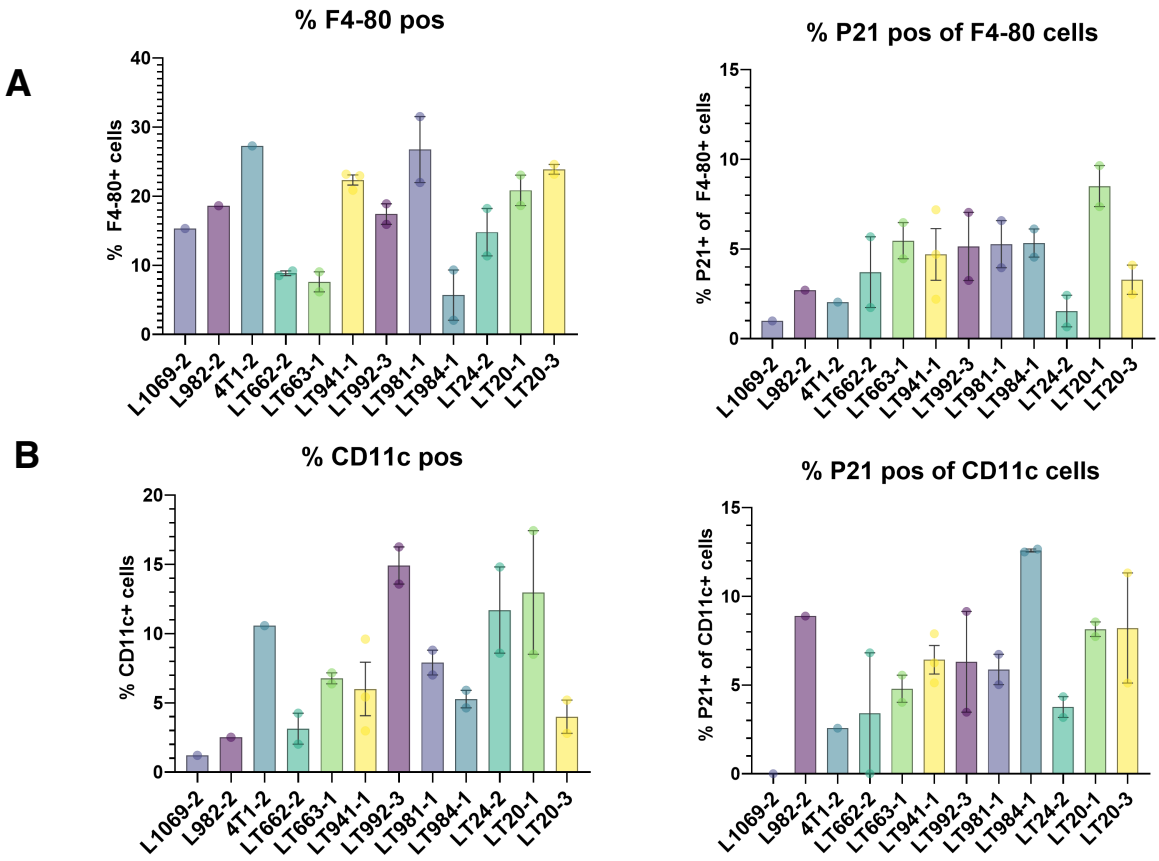
A
% F4-80 pos
% F4-80+ cells
% P21 pos of F4-80 cells
% P21+ of F4-80+ cells
B
% CD11c pos
% CD11c+ cells
% P21 pos of CD11c cells
% P21+ of CD11c+ cells
L1069-2
L982-2
4T1-2
LT662-2
LT663-1
LT941-1
LT992-3
LT981-1
LT984-1
LT24-2
LT20-1
LT20-3

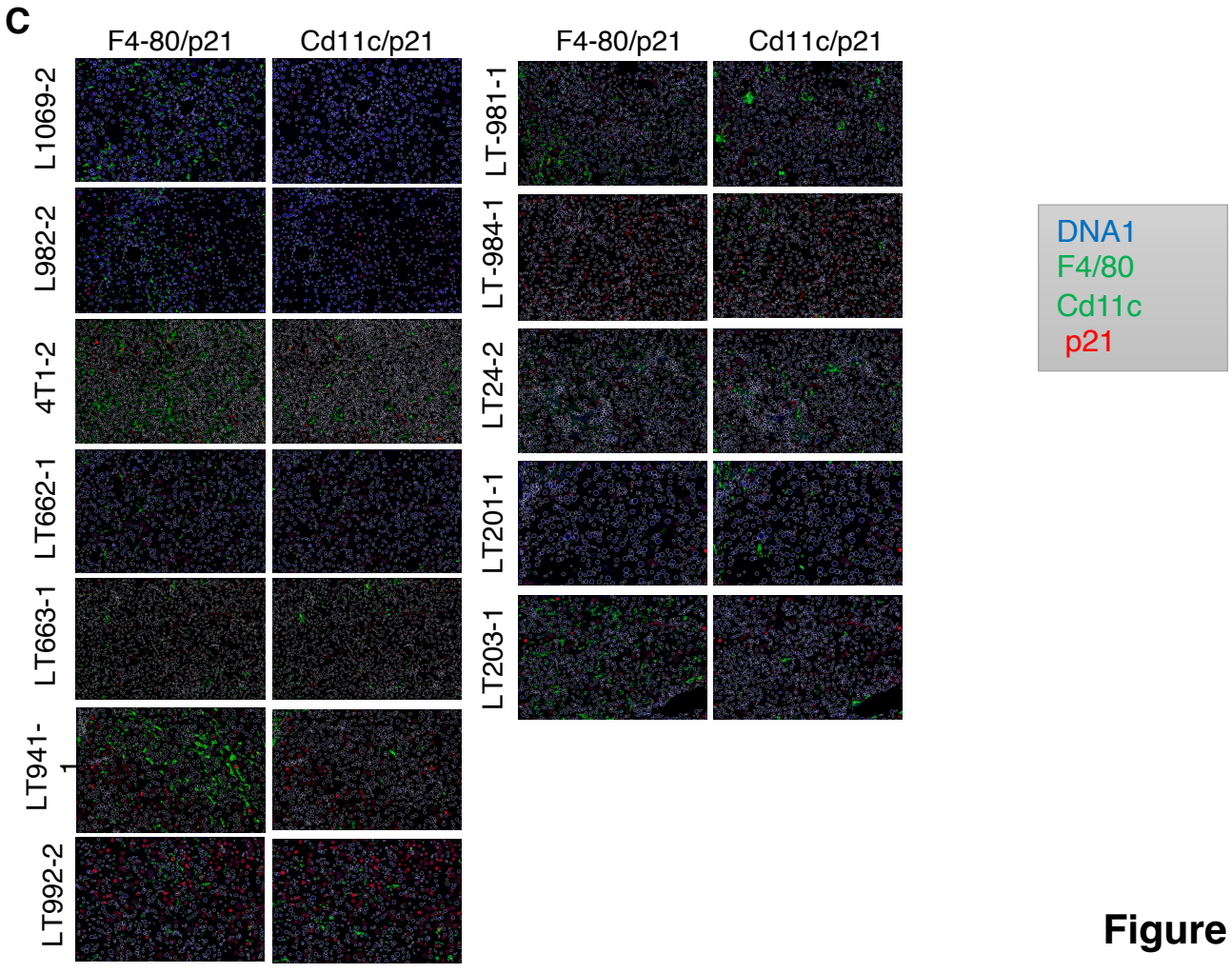
C
F4-80/p21
Cd11c/p21
L1069-2
L982-2
4T1-2
LT662-1
LT663-1
LT941-1
LT992-2
LT-981-1
LT-984-1
LT24-2
LT201-1
LT203-1
DNA1
F4/80
Cd11c
p21

Figure 9.